IEEE Access
Multidisciplinary ⋮ Rapid Review ⋮ Open Access Journal

Received 3 February 2023, accepted 25 February 2023, date of publication 3 March 2023, date of current version 10 March 2023.

Digital Object Identifier 10.1109/ACCESS.2023.3252360

TOPICAL REVIEW

Review of Flux-Weakening Algorithms to Extend the Speed Range in Electric Vehicle Applications With Permanent Magnet Synchronous Machines

CARLOS MIGUEL-ESPINAR, DANIEL HEREDERO-PERIS, ROBERTO VILLAFAFILA-ROBLES, (Member, IEEE), AND DANIEL MONTESINOS-MIRACLE, (Senior Member, IEEE)

Centre d'Innovació Tecnològica en Convertidors Estàtics i Accionaments (CITCEA), Departament d'Enginyeria Elèctrica, ETS d'Enginyeria Industrial de Barcelona, Universitat Politècnica de Catalunya, 08028 Barcelona, Spain

Corresponding author: Carlos Miguel-Espinar (carlos.miguel@upc.edu)

ABSTRACT This article reviews Flux-Weakening (FW) algorithms for Permanent Magnet Synchronous Machines (PMSMs), focusing on the automotive sector, especially in electric and hybrid electric vehicles. In the past few years, the spread of Electric Vehicles (EVs) has improved the technology of electric machines and their control to achieve more compact and competitive solutions. PMSMs are the most widespread electric machines used in EVs thanks to their high-power density and potential operation at constant power range during high speed. Such high speed implies a high electromotive force. An FW technique is mandatory to reduce the electromagnetic flux generated by the electric machine due to the voltage limits of the traction inverter and the energy source. This article classifies and analyses the state-of-the-art FW control strategies by comparing their main advantages and drawbacks. The Vector Current Control (VCC) method that regulates the modulus of the applied voltage is the most common one in the literature thanks to i) its robustness to parameter modification and model unsureness, ii) low computational complexity, and iii) high dynamic response and control stability.

INDEX TERMS Electric vehicles, flux weakening, maximum torque per voltage, motor control strategies, permanent magnet synchronous machines.

I. INTRODUCTION

Nowadays, the use of mild-hybrid and full-electric vehicles and micro-mobility vehicles is rapidly increasing, hence the importance of reducing Greenhouse Gas (GHG) emissions. Transportation is one of the industrial sectors that contribute the most to the GHG emissions, producing approximately 28% of the total amount [1], being road transportation the source of practically 75% of transport GHG emissions [2].

Electric powertrains offer highly efficient conversion of the energy stored in their power sources - such as batteries, ultra-capacitors, and fuel cells - into traction power for the wheels. The electric traction machines take the delivered electrical energy and convert it into motion through electromagnetic fields. Likewise, the electric machines transform the wheels' braking into electrical energy in the inverse process during braking. So, the electric engine and the power converter are the main actors for the bidirectional energy conversion, impacting the vehicle's average available power and efficiency.

Fig. 1 shows the demanded torque-speed characteristic of an electric machine in all speed ranges for EV applications, distinguishing between the constant torque and constant power regions [3]. High torque is required by quick acceleration, hill climbing, engine auto-start, and reversing at high road gradient at lower speeds. Besides, the electric powertrain should deliver a high torque for city driving at the medium-speed range. However, the electric machine should operate at a lower torque rate at the high-speed range.

The correct selection of the electric machine depends on several parameters such as vehicle architecture, engine size, drive cycles, space restrictions, maximum weight,

The associate editor coordinating the review of this manuscript and approving it for publication was Chandan Kumar.

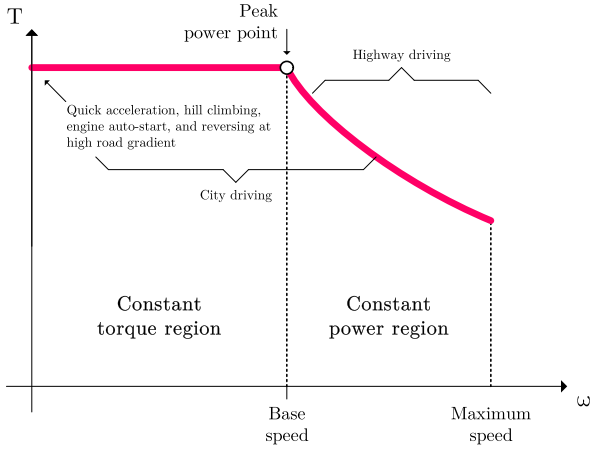

FIGURE 1. Qualitative torque-speed stationary characteristic for an EV and most frequent operating points based on [3].

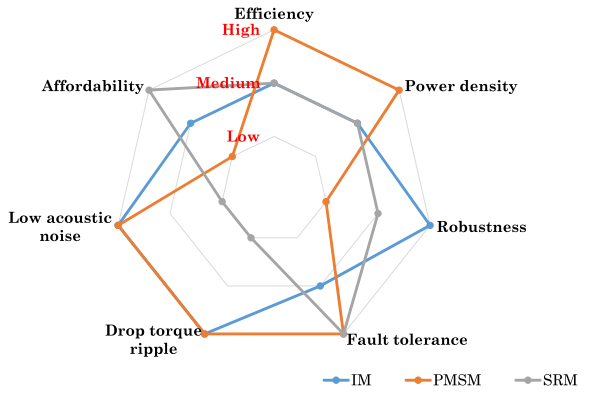

FIGURE 2. Comparison of the main features of IMs, PMSMs, and SyRMs technologies for EVs. Source: [4], [7].

lifetime, torque-speed characteristics, peak-power requirements, thermal and structural restraints, and noise-vibration-harshness (NVH) [3], [4], [5], [6]. There are several alternatives to optimize the traction machine design. Still, the most comprehensive solutions are classified as follows: i) Induction Machines (IMs), ii) Permanent Magnet Synchronous Machines (PMSMs) that can be subclassified as Interior Permanent Synchronous Machines (IPMSMs) and Surface Permanent Synchronous Machines (SPMSMs), iii) Synchronous Reluctance Machines (SyRMs), and iv) Wounded Rotor Synchronous Machines (WRSMs).

IMs, PMSMs, and SyRMs are compared in terms of efficiency, power density, robustness, fault tolerance, torque ripple drop, acoustic noise, and affordability in Fig. 2. Authors in [4] give specific numbers for each parameter. Nevertheless, the authors of this paper have qualitatively categorised them into three labels: low, medium, and high, the former and the latter meaning the worst and best results, respectively.

Although different electric machines are found in current EVs, the most common ones are PMSMs, and IMs [3], [7], [8]. Even so, in recent years, SyRMs have experienced a considerable increase in their penetration in the

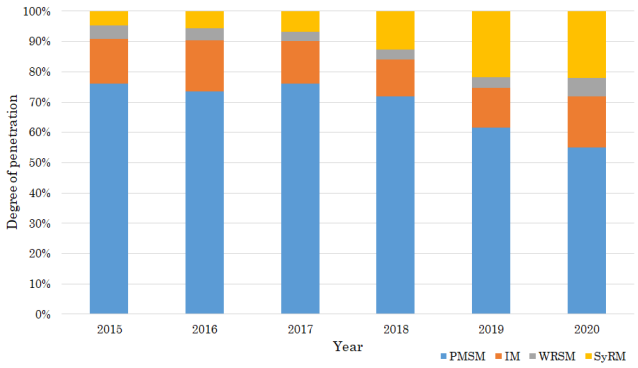

FIGURE 3. Degree of penetration of each type of electric machine in BEV and PHEV market. Source: [13].

EV market, as is shown in Fig. 3, due mainly to their low cost and independence of rare-earth magnets [9]. However, according to available data for BEVs and PHEVs in passenger cars (Fig. 3), EV manufacturers still prefer the PMSM option due to its high efficiency, superior power density, maturity and robustness. SPMSMs are employed when high power density is required, whereas IPMSMs are used for high-speed applications thanks to their FW capability, which is the case for EV applications [10].

Most electric vehicles still rely on Permanent Magnet (PM) radial flux Electric Machine (EM). However, the EU specifications regarding the massic vs volumic torque design of automotive EMs in 2020 are not reached. Axial flux EMs shows great potential to increase the performance of the electric powertrain. For example, the most efficient axial EM was developed by YASA, which proposed a PM axial flux EM achieving 11 N·m/kg and 41 N·m/l continuous torque and 2 kW/kg and 7 kW/l continuous power densities [11]. Another new and emerging technology is the Brushless Stator-Mounted Machines (BSSMs), with the so-called Flux Modulation (FM) effects, which use asynchronous field harmonics to realize energy conversion by altering the basic principles for conventional mechanic design, which requires the stator and rotor to have the same pole number [12]. This type of machine seems adequate for EV traction motors due to their suitability for high-seed high-torque density performance, as well as possessing suitable heat dissipation and flux weakening capabilities.

When it comes to efficiency, all speed ranges have to be contemplated. Although a vehicle used in urban zones has to prioritise the performance of the constant torque region, a vehicle for long journeys should consider the constant power region. As shown in Fig. 4, PMSMs have their best efficiency at low-medium speed range, whereas both IMs and SyRMs are preferable at high speeds and over a wider speed range compared with PMSMs. In this figure, each machine's area is depicted as equipotential lines that surround the range of an efficiency (η) superior to 85%. So, a PMSM could be preferred for urban areas, where vehicles are continuously starting and stopping, while IMs and SyRMs would be more efficient at high speeds [4].

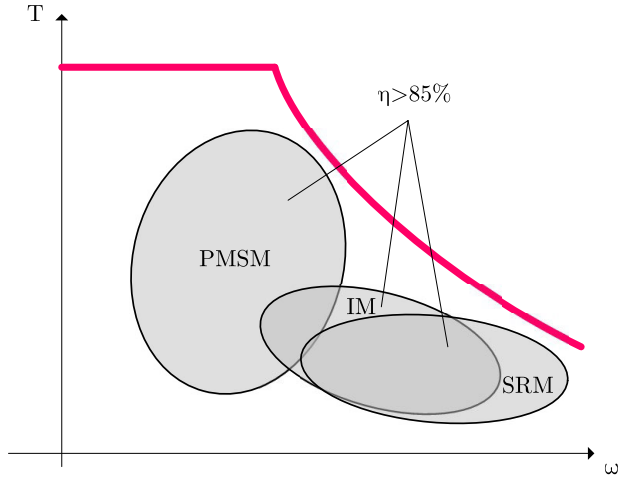

FIGURE 4. Qualitative efficiency maps of different machines both in the constant torque and constant power regions. Source: [7].

The global efficiency in the constant torque and constant power regions also depends on the control strategy and the other elements of the powertrain. Traditionally, control strategies have been focused on the electric machine. Nonetheless, the power source, power electronics, and the electric machine must be included to improve the entire powertrain efficiency. On the one hand, at low speeds, the current trajectory can be modified to the traditional ones if power semiconductors' switching and conduction power losses are considered [14]. On the other hand, a variable switching frequency at low speeds and a variable modulation strategy enlarge the speed ranges. The most standard and comprehensive solution to reduce losses is the Space Vector PWM (SVPWM) technique. However, Continuous and Discontinuous PWM (CPWM, DPWM) have been proposed in the literature, negatively affecting the Noise Vibration and Harness of the electric machine. Overmodulation with Noise Reduction (ONR) and Virtual Phase Compensation (VPC) are modulation strategies used to diminish the losses in all the speed ranges [15], [16].

The next electric machine generation will pursue several goals that can be summarized as [17]:

- Cost reduction through the use of new magnet materials or advanced configurations without rare-earth magnet dependency, but with similar flux density, and the simplification of the cooling system, where air-cooling is highly considered. Nowadays, the main drawbacks of rare-earth magnets are their scarcity, price fluctuations, and high cost.
- High efficiency through the development of high-performance alloys, for example, magnetic steels and copper alloys to reduce copper and iron losses.
- High power density thanks to increased speed operation and high-performance cooling for increased power capabilities.
- Improved motor design and development processes, considering a complete product life cycle assessment in a circular economy environment.
- Easy dismantling and recyclability.

Embedded software in electrified vehicles implements a real-time optimal control of the power flow between the power source and the load to maximize the energy system economy and drivability, the efficiency of the motor control, the optimization of battery performance and its protections, and the engine start/stop functionality, among others. The control algorithm is responsible for maximizing the electric drive system efficiency by choosing the electric machine's optimal operating point at low and high speeds, thus achieving the best performance of the machine in all speed ranges.

Some electronic control modules interact with sub-systems such as braking, heating, ventilation, and battery management in EVs. Nowadays, the traction inverter has the only functionality of controlling the electric machine both for positive (acting as a motor) or negative torque (acting as a generator), depending on the driver inputs through the accelerator and the brake pedal position. However, in micromoblity, the traction inverter itself has to interact with the different elements of the powertrain to carry out some high-level functions more straightforwardly.

Some of the features in the development of newer control algorithms for electric powertrain are summarized below as:

- Torque and speed algorithms that get the best efficiency from the electric machines plus the power electronics as a whole [14].
- Total Harmonic Distortion (THD) control of the current generated by the traction inverter or the torque ripple that generate losses in the powertrain [14].
- High-saturation-level consideration for PMSMs and SyRMs to achieve the best performance at high speeds. The inductance values of the machine vary nonlinearly under different operating conditions because the magnitude and phase angle of the applied current can change the magnetic flux distributions, and the saturation of magnetic materials in the motor can change the machine reluctance [18].
- Algorithms to automatically determine the parameters of the machine and use them to auto-tune the low-level controllers, considering the Flux-Weakening (FW) control [19].

This paper is structured as follows: in Section II, the necessity of an FW technique to maximise the performance of the electric machine is justified for EV applications. In Section III, a classification and an overview of the state-of-the-art FW control strategies are presented. In Section IV, the main advantages and disadvantages of the analysed methods are discussed. Finally, in Section V, the conclusions are drawn.

II. FLUX-WEAKENING NECESSITY

A. ATTAINABLE OPERATING POINTS

According to [10], the PMSM electrical dynamic equations referred to the synchronous rotor frame with the d-axis aligned to the rotor flux, and by implementing the Park transformation that maintains the current and voltage modulus

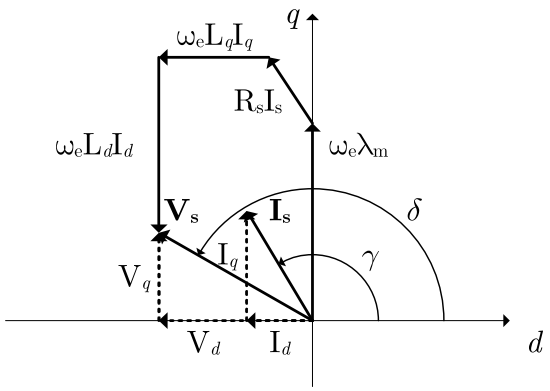

FIGURE 5. Phasor diagram in *dq*-axis.

invariant, are

$$\begin{bmatrix} v_d(t) \\ v_q(t) \end{bmatrix} = R_s \begin{bmatrix} i_d(t) \\ i_q(t) \end{bmatrix} + \begin{bmatrix} L_d & 0 \\ 0 & L_q \end{bmatrix} \begin{bmatrix} \frac{di_d(t)}{dt} \\ \frac{di_q(t)}{dt} \end{bmatrix} + \begin{bmatrix} 0 & -\omega_e L_q \\ \omega_e L_d & 0 \end{bmatrix} \begin{bmatrix} i_d(t) \\ i_q(t) \end{bmatrix} + \lambda_m \begin{bmatrix} 0 \\ \omega_e(t) \end{bmatrix}, \tag{1}$$

where $v_d(t)$, $v_q(t)$, $i_d(t)$ and $i_q(t)$ are the time-dependent voltage and current dq components, L_d and L_q are the motor inductance at the dq-axis, λ_m is the flux linkage due to the spinning of the magnets, R_s is the winding phase resistance and $\omega_e(t)$ is the time-dependent electrical speed.

At steady-state conditions, the voltage equations are simplified as

$$\begin{bmatrix} V_d \\ V_q \end{bmatrix} = R_s \begin{bmatrix} I_d \\ I_q \end{bmatrix} + \begin{bmatrix} 0 & -\omega_e L_q \\ \omega_e L_d & 0 \end{bmatrix} \begin{bmatrix} I_d \\ I_q \end{bmatrix} + \lambda_m \begin{bmatrix} 0 \\ \omega_e \end{bmatrix}, \tag{2}$$

where V_d, V_q, I_d and I_q are the non time-dependent voltage and current dq components, and ω_e is the non time-dependent electrical speed.

Fig. 5 represents the diagram phasor of the PMSM electrical derived from (2). I_s is the modulus current vector and V_s is the modulus voltage vector. It has to be noted that γ (current angle) and δ (voltage angle) are referred to the positive d-axis. In the literature, some algorithms to control the PMSM are based on the pair variables I_d and I_q and others on the pair variables I_s and γ. In Section IV, it is analysed the main advantage of the polar system versus the cartesian system.

The relationship between mechanical and electrical speed in a PMSM is expressed as

$$\omega_m = \frac{\omega_e}{pp}, \tag{3}$$

where ω_m is the mechanical speed, and pp is the pair of poles of the electric machine.

The electromagnetic torque (T_{em}) is expressed as

$$T_{em} = \frac{3}{2} pp(\lambda_m I_q + (L_d - L_q) I_d I_q). \tag{4}$$

Achievable operating points are restrained according to the current and voltage limits. The maximum available current ($I_{s,max}$) is expressed as

$$\sqrt{I_d^2 + I_q^2} = I_s \leq I_{s,max} = \min\left\{I_{motor,max}; I_{inv,max}; I_{source,max}\right\}, \tag{5}$$

where $I_{motor,max}$ is the maximum motor current, $I_{inv,max}$ is the maximum inverter current, and $I_{source,max}$ is the maximum power source current. One of the main parameters of PMSMs is the short-circuit current (I_{sc}) of the machine. This current represents the flux generated in the stator by the winding currents with the same direction (in the dq-axis phase diagram) and value as the flux linkage of the permanent magnets. $I_{s,max}$ can be higher or less than I_{sc}, depending on whether the electrical and thermal battery, inverter, and power source limits are higher or lower than I_{sc}. This feature will define the possibility to extend the torque-speed characteristic at high speeds.

The maximum available voltage ($V_{s,max}$) is formulated as

$$\sqrt{V_d^2 + V_q^2} = V_s \leq V_{s,max} = \frac{V_{source,max}}{\sqrt{3}}, \tag{6}$$

where $V_{source,max}$ is the power source voltage. A Space Vector Pulse Width Modulation (SVPWM) strategy is considered in this article. Neglecting the resistor voltage drop of (2), (6) yields to

$$\frac{(I_{sc} + I_d)^2}{\left(\frac{1}{L_d}\right)^2} + \frac{I_q^2}{\left(\frac{1}{L_q}\right)^2} \leq \left(\frac{V_{s,max}}{\omega_e}\right)^2. \tag{7}$$

Fig. 6 depicts the characteristic curves for an SPMSM and an IPMSM. The current limit (5) is seen as a circle centered in the coordinates (I_d,I_q) = (0,0), with a radius equal to $I_{s,max}$. The voltage limit (7), in the case of an SPMSM, depicts a circle centered in the coordinates (I_d,I_q) = (-I_{sc},0) and with a radius equal to $\frac{V_{s,max}}{L_d \omega_e}$. In the case of an IPMSM, (7) describes an ellipse with the same center, in which semi-major and semi-minor axes are equal to $\frac{V_{s,max}}{L_d \omega_e}$ and $\frac{V_{s,max}}{L_q \omega_e}$, respectively. If the stator resistance is considered, the voltage ellipses are deformed, and the major axis of the ellipses are no longer parallel to the d-axis [20], [21]. The torque curves, in the case of SPMSMs, are straight lines which only depend on the I_q values as it is described in (4) with $L_q = L_d$. Nevertheless, in the case of IPMSMs, the torque curves are rectangular hyperbolas according to (4) with $L_q \neq L_d$.

B. LOW-BACK ELECTROMOTIVE FORCE CHARACTERISTIC CURVE

One of the primary limiting features of PMSMs is their limited excitation voltage to achieve compact designs. The electric machine's Back Electromotive Force (BEMF) proportionally increases with the mechanical speed due to the magnetic field generated by the permanent magnets when the machine rotates. Generally, the operation of a PMSM can be distinguished in two different zones, depending on the

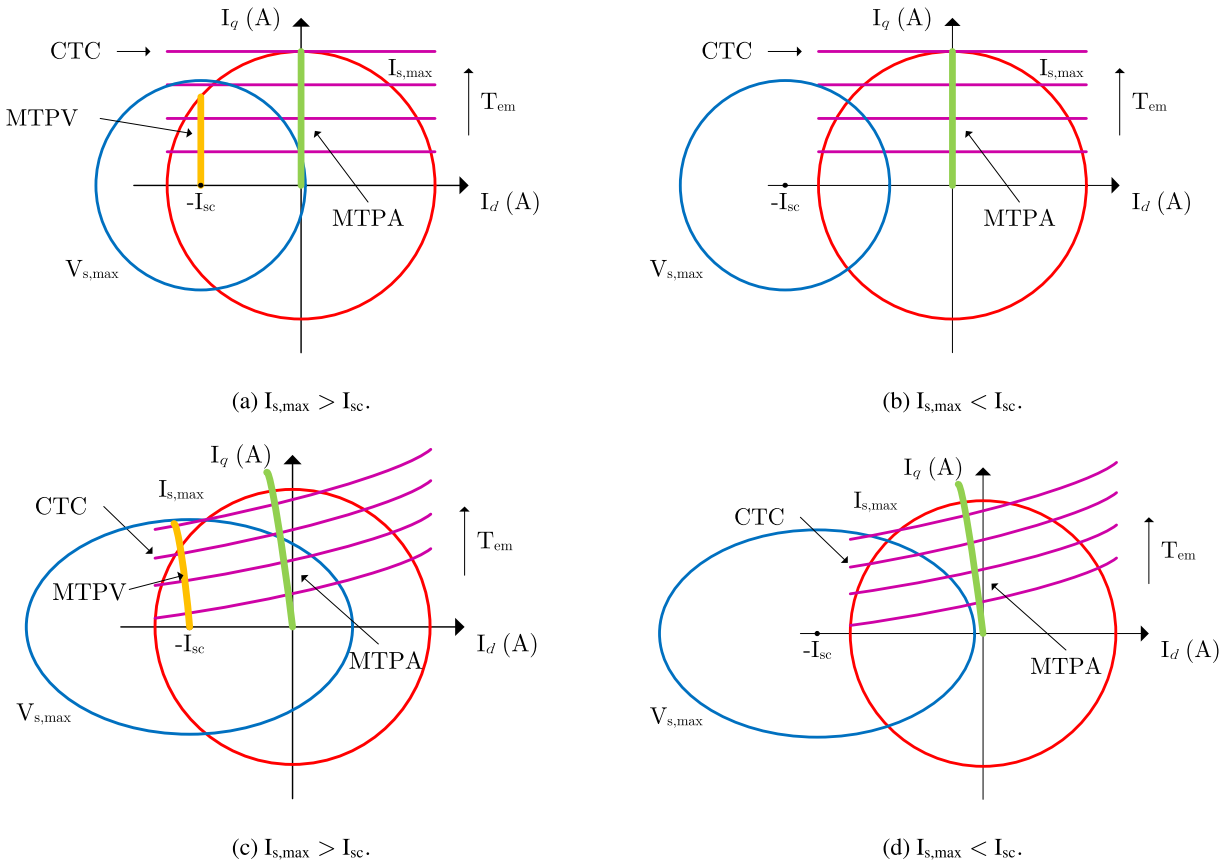

FIGURE 6. Characteristic curves for SPMSMs and IPMSMs. The red line represents the current limit circle. The blue line is the voltage limit ellipse. The magenta lines illustrate the constant torque hyperbolic curves during the Constant Torque Control (CTC). The green line depicts the Maximum Torque Per Ampere (MTPA) hyperbolic curve. The yellow line is the Maximum Torque Per Voltage (MTPV) hyperbolic curve.

value of the BEMF, the stator winding voltage drop, and the maximum current and voltage applied to the machine. On the one hand, if the BEMF plus the stator winding voltage drop is lower than the maximum voltage synthesised by the traction inverter, the electric machine is working in the first zone called Low Back Electromotive Force (LBEMF). However, when the speed continues to increase, the limit voltage of the traction inverter is reached, and the electric machine is then said to have entered the FW zone. From that moment on, the voltage applied to the electric machine should be adjusted throughout the current circulation through the stator windings to be compatible with the available DC voltage to increase the mechanical speed while a mechanical torque is still applied to the shaft.

In [10, p. 303-327] some strategies at the LBEMF zone have been compared: Constant Torque Angle Control (CTAC), Unit Power Factor Control (UPFC), Constant Stator Flux Control (CSFC) and Maximum Torque Per Ampere (MTPA). In general, for EV applications, the MTPA algorithm is chosen to minimise the current needed for the demanded torque. This decision is supported by the necessity of in-vehicle applications to reduce the cable conductors' cross-sectional area and maximise the efficiency of the powertrain.

The MTPA condition for PMSMs is defined as $\frac{\partial T_{\text{em}}}{\partial \gamma} = 0$, expressing (4) in terms of I_{s} and γ, instead of I_d and I_q. Neglecting the magnetic saturation of the electrical sheets, the MTPA angle value (γ_{MTPA}) is expressed as

$$\gamma_{\text{MTPA}} = \frac{\pi}{2} \quad \text{or} \tag{8}$$

$$\gamma_{\text{MTPA}} = \arccos\left(\frac{-\lambda_{\text{m}}}{4 \cdot I_{\text{s}} \cdot \left(L_d - L_q\right)} - \sqrt{\frac{1}{2} + \frac{\lambda_{\text{m}}^2}{16 \cdot I_{\text{s}}^2 \cdot \left(L_d - L_q\right)^2}}\right), \tag{9}$$

which are represented in a green straight curve in Fig. 6a and Fig. 6b for SPMSMs (8) or in a green hyperbolic curve in Fig. 6c and Fig. 6d for IPMSMs (9), respectively.

C. FLUX-WEAKENING CURVES

A constant power range, the elimination of multiple mechanical gear systems, reduction of the volt-ampere controller rating, and a compact design are desirable for EV applications [22], and the FW operation can achieve this performance.

Fig. 7 shows the ideal torque-speed and power-speed curves for a PMSM without considering power losses

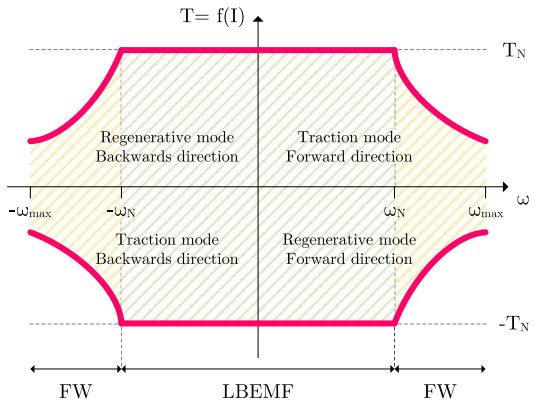

(a) Torque versus speed.

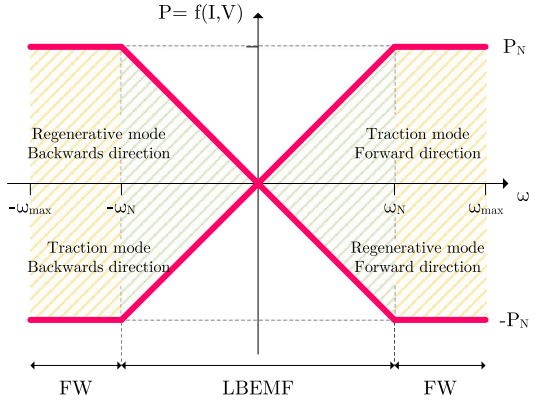

(b) Power versus speed.

FIGURE 7. Torque-speed and power-speed curves for a PMSM both in traction and regenerative mode. The LBEMF zone is shown in green, whereas the FW zone is illustrated in yellow.

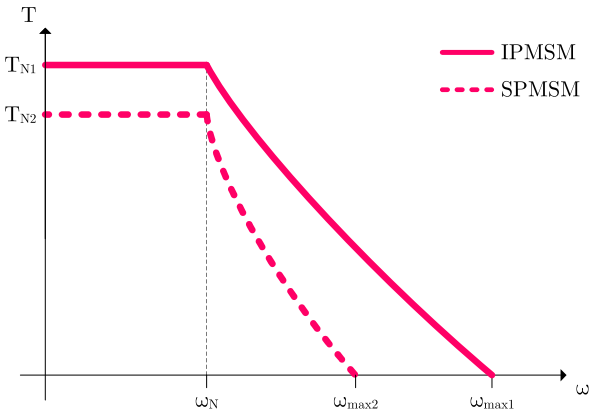

(a) Torque versus speed.

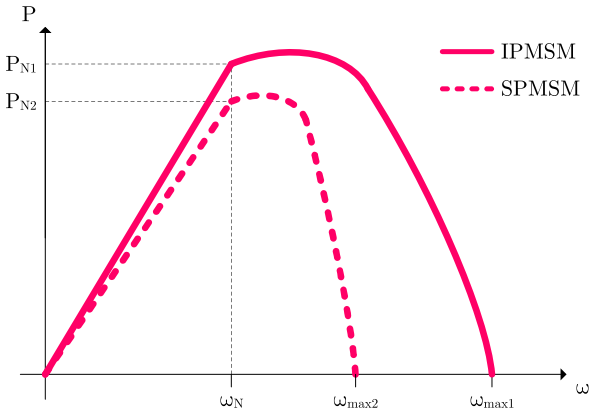

(b) Power versus speed.

FIGURE 8. Torque-speed and power-speed curves comparison for an SPMSM (dashed magenta line) and IPMSM (continuous magenta line).

(copper, iron or mechanical losses). These graphs are represented in the traction and regenerative braking modes when the vehicle is moving forward or backward. The nominal torque (T_N) is defined as the torque value sustained by the electric machine without any danger of damage, related mainly to the nominal current (I_N). At the same time, the rated power is defined as the power value indefinitely maintained by the electric machine without any threat to the device, which depends on the nominal current and voltage (V_N).

The traction inverter can maintain the nominal torque of the electric machine until the mechanical speed achieves the rated value (ω_N). At this moment, the stator winding voltage reaches its nominal value, which in turn is the nominal synthesised voltage by the traction inverter, and depends on the actual voltage of the power source (V_{source}) and the switching strategy. All possible working points inside the green striped area belong to the LBEMF zone. From that point on, if the speed continues to rise, the applicable torque will be lower than the nominal value, and the current vector should be modified to maintain the stator voltage equal to the maximum value synthesisable by the traction inverter, so it works in the FW zone that is depicted by the yellow striped area. The maximum controllable speed will depend on the maximum current and voltage limits permitted by the power source, the traction inverter, and the electric machine, and the maximum mechanical speed due to the bearings and the gear system.

In a solid magenta line, Fig. 8 shows the torque-speed and power-speed characteristics for an IPMSM with the rated torque and power equal to T_{N1} and P_{N1}, respectively, and in a dashed magenta line the same characteristics for an SPMSM with the rated torque and power equal to T_{N2} and P_{N2}, respectively. An IPMSM has a nominal torque higher than an SPMSM thanks to its reluctance torque, considering the same characteristic parameters. An IPMSM can take advantage of the FW behaviour thanks to the difference between reluctance in its magnetic circuit from the nominal speed to the maximum speed. Nevertheless, the range of FW for SPMSMs is more limited than for IPMSMs. Their maximum speed is defined by the inductance of the electric machine, which generally is lower than for IPMSMs. Although SPMSMs can adopt fractional slots concentrated windings that increase the inductance of the electric machine significantly and therefore can offer a decent FW range, still lower than the IPMSMs.

Fig. 9 shows the capability of the deep FW region depicted in solid yellow if the Maximum Torque per Voltage (MTPV) zone exists. This zone is also known as Maximum Torque per Flux (MTPF), and it maximises the machine's torque per the stator flux. The MTPV zone is only achievable if the condition $I_{s,max} > I_{sc}$ is satisfied. Ideally, the electric machine delivers torque until an infinite speed if no losses and mechanical limitations are considered. Nevertheless, the maximum speed is finite due to copper, iron and mechanical losses. However, if the MTPV zone is not applied, the maximum theoretical achievable speed is limited. From the power perspective, the MTPV region can achieve more power during the deep FW performance, theoretically reaching a constant power (P_{MTPV}). This figure reveals the importance of the control algorithm in PMSM applications since it is crucial to obtain more power from the same electric machine.

If the electric machine works in the MTPV region, up to the maximum speed defined by the current and voltage limits, for a certain speed value the torque obtained from the machine is higher than what it would be if an algorithm that only took into account the current and voltage limits were to be considered, as it is shown in Fig. 9. So, this means that for the same torque value the magnet will be less demagnetised, because the d-axis current will be lower.

The MTPV trajectory is defined as the curve where the maximum torque at minimum current is achieved, considering the voltage limit. The MTPV condition for PMSMs is defined as $\frac{\partial T_{em}}{\partial \delta} = 0$, expressing (4) in terms of I_s and δ. Neglecting the magnetic saturation of the electrical sheets, the MTPV current value (I_{MTPV}) is expressed for SPMSMs and IPMSMs, respectively, as

$$I_{MTPV} = \frac{I_{sc}}{\cos(\gamma)} \quad \text{and} \tag{10}$$

$$I_{MTPV} = \frac{\mu \cdot \cos(\gamma)}{2 \cdot \left(\cos^2(\gamma) - \xi^2 \cdot \sin^2(\gamma)\right)} + \frac{\sqrt{\mu^2 \cdot \cos^2(\gamma) - \left(\cos^2(\gamma) - \xi^2 \cdot \sin^2(\gamma)\right) \cdot \left(\mu^2 - \xi^2 \cdot \beta^2\right)}}{2 \cdot \left(\cos^2(\gamma) - \xi^2 \cdot \sin^2(\gamma)\right)}, \tag{11}$$

where ξ is the saliency ratio defined as $\frac{L_q}{L_d}$, and μ and β are defined as

$$\beta = \frac{\lambda_m}{L_q - L_d}, \tag{12}$$

$$\mu = \beta - \frac{\lambda_m}{L_d}. \tag{13}$$

If the voltage curve center is located inside the current circle ($I_{s,max} > I_{sc}$), then the theoretical maximum achievable speed is infinite, as long as the MTPV curve is followed and no electromagnetic and mechanical losses are considered. This is represented in yellow as a straight curve in Fig. 6a for SPMSMs or as a hyperbolic curve in Fig. 6c for IPMSMs.

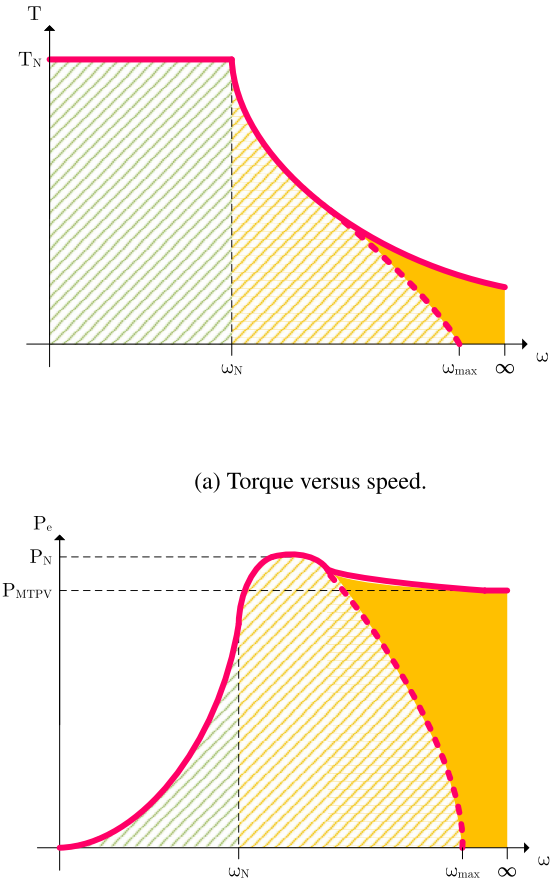

(a) Torque versus speed.

(b) Power versus speed.

FIGURE 9. Comparison of torque-speed and power-speed curves with and without the MTPV zone. The LBEMF zone is represented in green stripes, the first region of the FW zone is shown in yellow stripes, and the extended FW region is illustrated in solid yellow.

On the contrary, if the voltage curve center is located outside the current circle ($I_{s,max} < I_{sc}$), then the maximum speed is finite at the point $(I_d, I_q) = (-I_{sc}, 0)$, and there is no MTPV curve available as shown in Fig. 6b for SPMSMs and Fig. 6d for IPMSMs.

D. PERMANENT MAGNET SYNCHRONOUS MACHINE TRAJECTORIES

When the speed is low and the torque increases, the operating points move along the MTPA curve to minimise the stator current. The voltage ellipse curves shrink as the speed increases, and when the voltage ellipse curve crosses the MTPA zone, an FW strategy has to be applied, maintaining the stator voltage inside its limit. Depending on the torque reference, this value can be sustained at the FW during a specific speed range whenever the current limit is not reached. This particular region is named Constant Torque Control (CTC). If the speed increases and the voltage ellipse curves shrink and cross the current limit circle, the operating points

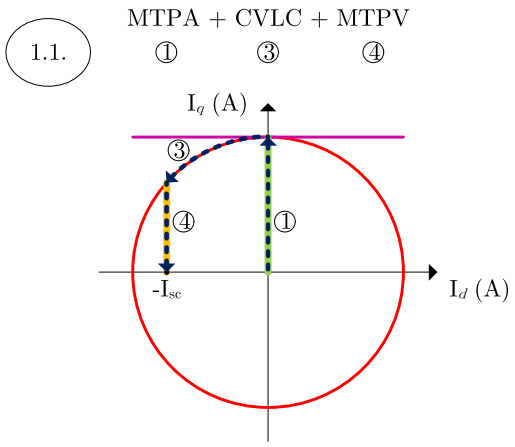

(a) Trajectory 1.1.

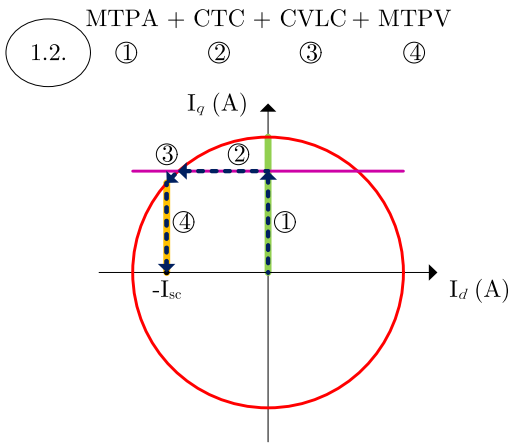

(b) Trajectory 1.2.

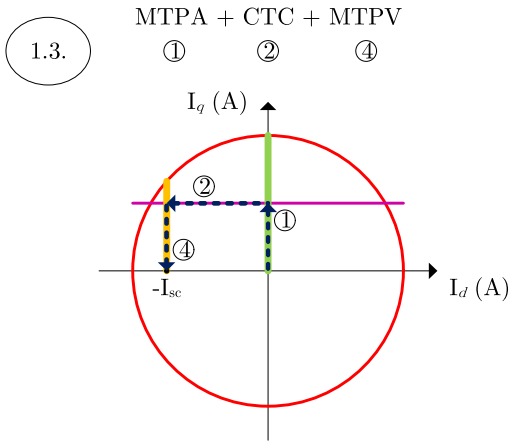

(c) Trajectory 1.3.

FIGURE 10. Trajectories at MTPA and FW zones for SPMSMs if $I_{s,max} > I_{sc}$.

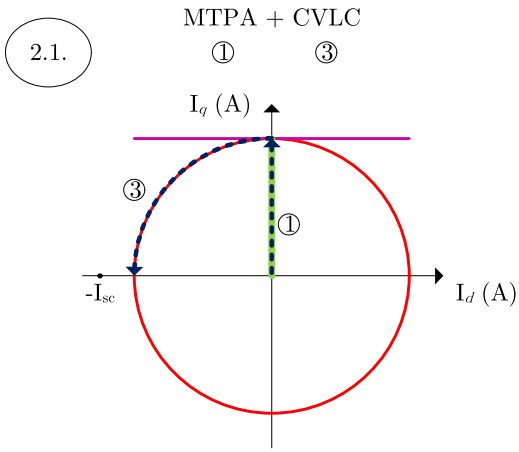

(a) Trajectory 2.1.

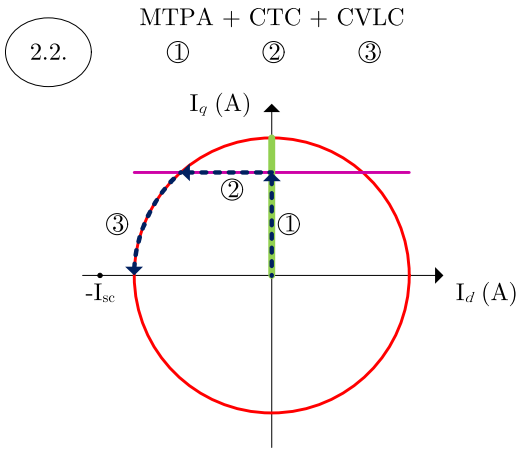

(b) Trajectory 2.2.

FIGURE 11. Trajectories at MTPA and FW zones for SPMSMs if $I_{s,max} < I_{sc}$.

move along the current limit circle. This particular region is called Current and Voltage Limit Control (CVLC). If the MTPV curve exists and the speed increases, the moment the current limit circle intersects the MTPV curve, the operating point will move along the MTPV curve.

Depending on the value of $I_{s,max}$, different trajectories can be followed. If $I_{s,max} > I_{sc}$, then the motor can follow either trajectory 1.1, 1.2 or 1.3, as it is depicted in Fig. 10. However, if $I_{s,max} < I_{sc}$, the electric machine can only follow trajectory 2.1 and 2.2, as it is showed in Fig. 11. All these figures are represented for SPMSMs. A similar approach can be made in the case of an IPMSM, whose characteristic curves are shown in Fig. 6c and Fig. 6d.

E. POWER LOSSES AND EFFICIENCY SIMULATION DURING FW OPERATION

The power losses on a PMSM depend on the Joule effect, magnetic losses in the stator and rotor electrical sheets, eddy current losses within the permanent magnets, and mechanical losses. In this section, all these possible losses are reduced to the Joule effect losses to compare the FW methods that work on the FW operation at the CVLC trajectory and the others that work in the CVLC plus MTPV trajectories. Simulations

TABLE 1. Characteristic parameters of the IPMSM.

Symbol	Description	Value	Unit
R_s	Stator resistance	17	mΩ
L_d	d-axis inductance	70	μH
L_q	q-axis inductance	79	μH
$V_{\text{ph-n,max}}$	Peak voltage	27.7	V
$I_{\text{ph,max}}$	Peak current	330	A
$\lambda_{\text{m,ph-n,max}}$	Peak flux-linkage	0.023	(V·s)/rad
pp	Pair of poles	20	
$T_{\text{m,n}}$	Rated torque	66	N·m
$\omega_{\text{m,n}}$	Rated speed	510	rpm

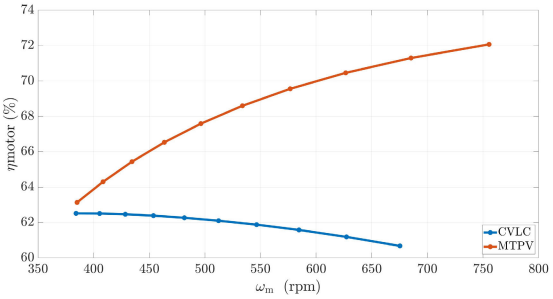

FIGURE 12. Motor Joule power losses regarding mechanical speed differentiating between CVLC and MTPV trajectory.

from a MATLAB-Simulink model are carried out to analyse the power losses and the efficiency of a direct-drive IPMSM, which runs as the rear wheel of an e-motorbike. The most relevant parameters of the electrical machine are listed in Table 1.

The PMSM is simulated under different load torque conditions: from 100 N·m to 180 N·m in steps of 10 N·m. Furthermore, the steady-state points depend on the control strategy that changes between the CLVC and MTPV trajectories. In the following graphs, the blue and orange lines represent the CVLC and MTPV trajectories. Fig 12 and Fig 13 show the motor joule power losses and efficiency regarding the mechanical speed in both trajectories. The first conclusion is that the MTPV trajectory can achieve a higher speed for the same torque load. Furthermore, for the same torque load, the power losses are less in the case of the MTPV trajectory than in the case of the CVLC trajectory. The main reason is that following the MTPV trajectory, the PMSM can apply the same torque as the CVLC trajectory but at a lower current rate.

III. FLUX-WEAKENING STRATEGIES

A. INTRODUCTION

Although several torque-and-speed regulation schemes are found in the scientific literature, such as Direct Torque Control (DTC) [23], [24], Field-Oriented Control (FOC) is the most used one, and it is widely accepted for PMSM control in the industry sector. In the case of DTC, the control variables are flux and torque, and its main advantages are simplicity, fast dynamic response and dependency to fewer parameters compared to the FOC schemes [25]. Nevertheless, the main problem of DTC is to determine the optimal flux and torque set values regarding the optimal efficiency and the consideration of the current and voltage limitations.

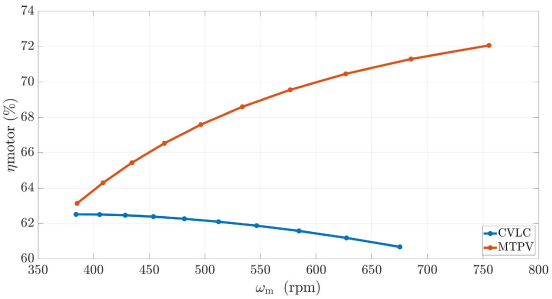

FIGURE 13. Motor efficiency regarding mechanical speed differentiating between CVLC and MTPV trajectory.

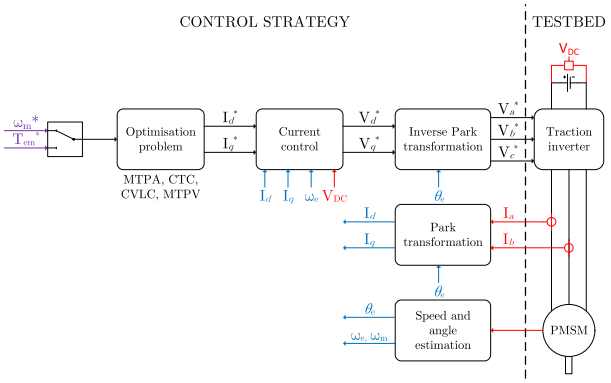

FIGURE 14. General block diagram implementing an FOC algorithm for PMSM applications by taking into account the FW region. The reference values are represented in purple. The feedback values from the real system are shown in red. The intermediate calculations are depicted in blue.

Some authors implement 2D-Look-Up Tables (LUTs) from experimental results or Finite Element Analysis (FEA) to get these values [23].

The main reason why FOC is used is its good dynamic performance, a moderate computational burden, and a constant switching frequency independent from the machine speed [26]. This method provides a decoupled torque and flux control during transients and steady-state for SPMSM. One of the main drawbacks of the FOC algorithm is the decoupling dependence to the plant parameters, such as the inductance winding and the flux-linkage, to get a high dynamic response when the torque reference changes. Moreover, for an IPMSM, there is no clear separation between flux and torque throughout the winding currents, and FW operation demands a minimum amount of voltage reserve due to the transients and compensates for any disturbances. The latter condition supposes a limit to the maximum power of the powertrain.

The general scheme in the synchronous reference frame of the PMSM control while using FOC and taking into account the FW zone is shown in Fig. 14. Depending on the application, some authors have implemented their FW algorithm by calculating the dq-axis current references from the torque or speed setpoint. Although each method is different, the MTPA algorithm is generally used in the LBEMF zone for EV applications, as mentioned in Section II. Furthermore, the torque equation plus the current and voltage

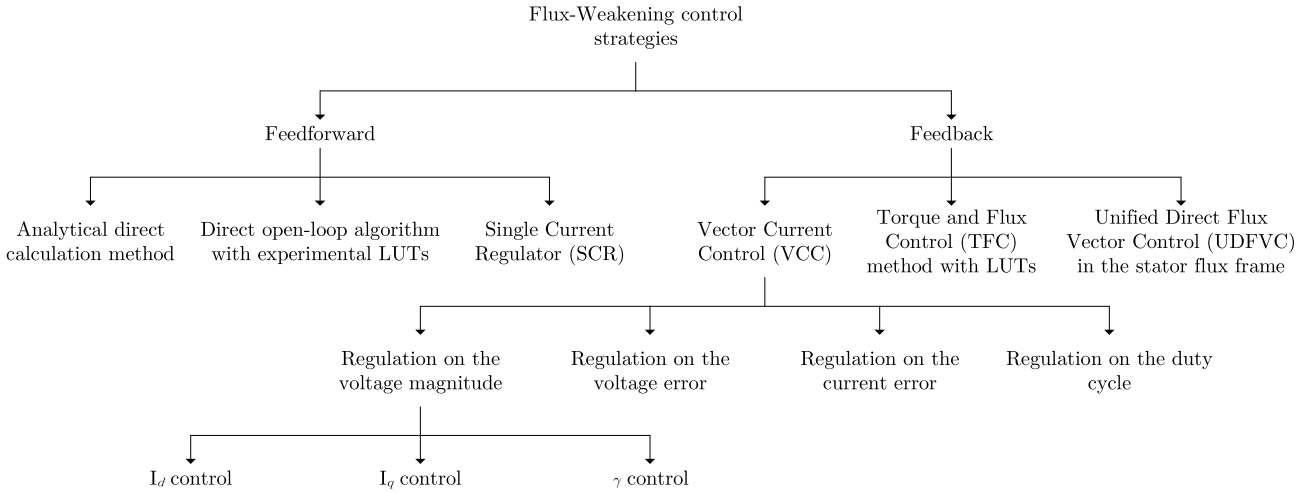

FIGURE 15. Control strategies for FW operation.

limits are considered during high speed. Additionally, some authors consider the MTPV region in the control structure. In summary, the FW operation follows an optimisation problem where the dq-axis current references should be determined from the torque or speed setpoint, considering the reference torque, current speed, current and voltage limits, and thermal state of the powertrain.

The hardware architecture is simple because it is formed by a DC power source, a Voltage Source Inverter (VSI), and a PMSM. Generally, the current values of the DC power source voltage, the phase currents (usually the neutral point is not connected, so only two current measurements are needed), and the electrical speed are required to implement the control. These feedback measurements are depicted in red. Some authors have proposed obtaining the mechanical speed from observers based on the plant model, and no speed sensor is needed [27], [28], [29], [30], [31]. For low-cost applications, Hall-effect switch sensors are used, but an accurate mathematical algorithm is required to obtain the correct electric speed and position [28], [29], [30], [31], [32], [33], [34], [35], [36], [37], [38], [39], [40], [41]. Intermediate calculations, depicted in blue, are needed to apply the control algorithm to calculate the actual currents in the machine's synchronous reference and the electrical speed and angle.

In the event that the speed controller is implemented, there is a control algorithm structure based on two cascade controllers: current and speed control loops. Generally, both a torque reference and a maximum speed limitation can be distinguished in most EV applications. The references to the control algorithm are shown in purple. Usually, a reference torque (T^*_{em}) is demanded through the accelerator pedal, and a maximum speed (ω^*_{m}) is established for the Cruise Speed Limiter (CSL).

The current and speed controllers can be individually parametrised through some well-known control techniques from the dynamic response, noise and disturbance rejection points of view because the dynamics of both are very different. In turn, traditional FOC algorithms apply two independent current controllers, i.e., one for the d-axis current regulation and the other for the q-axis current regulation. In the FW operation, the saturation of the two current regulators has to be avoided because they can conflict with each other, leading to instability of current [42].

B. FLUX-WEAKENING ALGORITHMS CLASSIFICATION

The literature reveals several FW control strategies, although there are no unified criteria to be classified. The purpose of this paper is to establish a basis for categorising them. Authors in [43] and [44] made the first approach, organising the FW methods into feedforward and feedback strategies. On the one hand, feedforward strategies are mentioned as model-based methods because they utilise the motor parameters and the current DC voltage to calculate the optimal current trajectories for the required torque and flux at each speed. The q-axis reference current is determined from the speed or torque command, and the d-axis reference current is obtained from the current and voltage constraints in different speed regions as a function of the operating speed. Feedforward methods depend highly on motor parameters and operating conditions, but guarantee good stability and transient responses [45].

On the other hand, feedback strategies are generally based on the direct control of the inverter output voltage through a proper control loop regulation. The d-axis reference current is adjusted to track the voltage limit at increasing speed. These methods are robust because they do not use the electric machine parameters. Nevertheless, the transient performance of closed-loop voltage controllers is poor, and the gain setup of the regulators is complex owing to the operation in the proximity of voltage saturation region [45].

Taking a step forward, authors in [46] have classified the FW control strategies into several groups (see Fig. 15). From the authors' best knowledge, Table 2 indicates the reviewed literature in this article differentiating those methods that

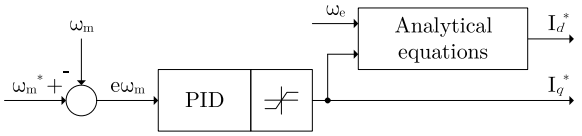

FIGURE 16. Block diagram of the analytical direct calculation method. Source: [48].

consider the deep FW operation from those methods that do not consider it.

Each method is described in the following sub-sections through a block diagram, and their main advantages and disadvantages are presented to establish a comparison. Thus, the FW capability will be the main focus of this analysis.

C. ANALYTICAL DIRECT CALCULATION METHOD

The analytical direct calculation method uses the equations in both LBEMF and FW zones to generate the required d-axis and q-axis reference currents through a flowchart diagram [20], [21], [45], [47], [48], [49], [50], [51]. The reference currents are calculated by considering the reference torque, actual speed, current limit, and voltage limit at every rate of the machine. When the speed is below the base speed, the electrical machine works in the LBEMF zone, applying the MTPA formula. When the speed is higher than the base speed, the electrical machine works at the voltage limit in the FW zone. In general, these equations do not consider either the stator resistance or the magnetic saturation to facilitate the implementation in a real system.

Fig. 16 shows a block diagram example to implement the analytical direct calculation algorithm with an FW operation. Generally, a PID speed controller generates the q-axis reference current, and the d-axis reference current is calculated from the electrical speed and the q-axis reference current using the characteristic equations of a PMSM. Fig. 17 shows the flowchart used to transition over the basic speed by calculating the d-axis current reference in case the electric machine is working in the LBEMF or FW zone.

The main drawback of this algorithm is its inherent susceptibility to the variation of the electric machine parameters and the required time to calculate the dq-axis current references in a real-time control when working with an IPMSM [63], [81]. Furthermore, these methods generally do not consider the magnetic circuit's stator resistance or saturation effects, making the control susceptible to becoming unstable in the worst situation. However, this simplification is only appropriate for high-power machines with relatively small stator resistance [101]. Sainz et al. presented a methodology in [21] to consider the stator resistance in the analytical expressions to generate the reference currents with low execution time, allowing their exact computing that avoids complex equations, LUTs or numerically adjusted polynomials. They claim that their method considers any parameter variation during real-time operation, and they propose linking this methodology with a parameter estimator strategy to obtain the best possible performance. In [20], Olarescu et al. combine a

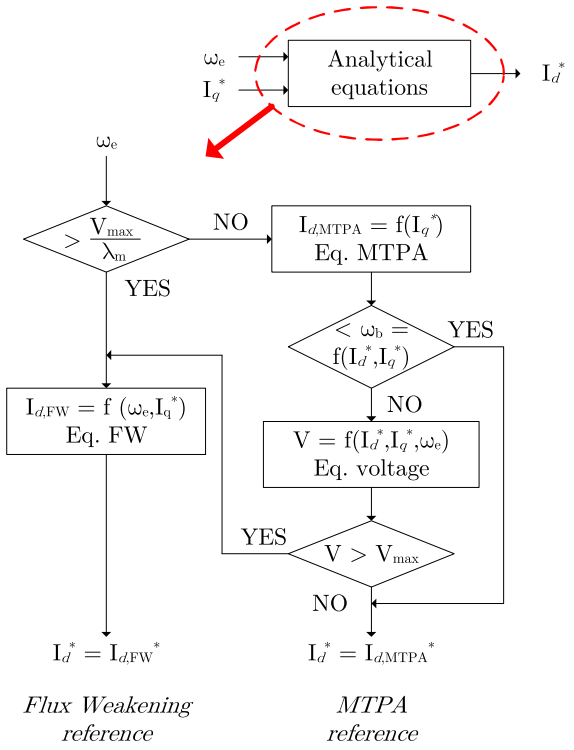

FIGURE 17. Flow chart of the analytical direct calculation method. Source: [48].

flowchart with the capability of working in the MTPV zone with a voltage PID controller to calculate the variation of the d-axis reference current taking into account the value from the reference torque. In [45], Tursini et al. implement a control strategy accounting for resisting voltage drop, simplifying the algorithm through piecewise-linear functions. In [51], Wang et al. propose a flowchart tree to decide the operation region regarding the current speed and the reference torque. Besides, a second-order Newton-Rapshon method based on a First-Order Taylor series Jacobian matrix approximation is used to calculate the pair dq-axis current references in an iterative form. Furthermore, they considered the magnetic cross-coupling, magnetic saturation, and non-linear differential inductances through LUTs.

D. DIRECT OPEN-LOOP ALGORITHM WITH EXPERIMENTAL LUTs

The direct open-loop algorithm method is based on experimental or FEA LUTs that store the relationship between the torque setpoint and the maximum allowable flux-linkage with the dq-axis current references [52], [53]. Fig. 18 shows the basic block diagram. In this case, the method to calculate the current references is not based on mathematical equations but offline LUTs. The extension from the base speed is achieved thanks to mapping the flux linkage and torque regarding the dq-axes currents setpoints and the minimum value between the optimal flux for the torque setpoint and the maximum flux according to the actual electrical speed.

TABLE 2. Control strategies for FW operation without and with MTPV operation.

Method	Without MTPV	With MTPV
Analytical Direct Calculation method	[45], [47]	[20], [21], [48]–[51]
Direct Open-Loop algorithm with experimental LUTs	[52]	[53]
SCR	[42], [54], [55]	[56]
VCC	[43], [57]–[69]	[46], [70]–[86]
TFC method with LUTs	[87], [88]	[89]–[98]
UDFVC in the stator flux frame	[99], [100]	-

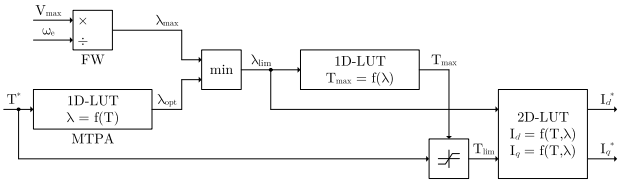

FIGURE 18. Block diagram of the direct open-loop algorithm with experimental or FEA LUTs method.

The main advantage of using LUTs to determine the current references is that they accounts for the inductance variability due to the magnetic saturation. In this way, the traction inverter can follow the torque reference continuously regardless of the degree of magnetic sheet saturation.

Its primary drawbacks are the sizeable experimental setup to obtain the different LUTs in the torque-speed range and the memory usage to store the LUTs in the traction inverter. Furthermore, the testing of the electric machine is risky and time-consuming. In [53], Kunter et al. assert a new control strategy relying on LUTs only containing points on the edges of the operating area. They ensure this method maintains a sufficient level of accuracy and minimizes the storage requirements and determination effort. Besides, they use the Newton-Rapshon algorithm based on the analytical machine equation and its average parameters to determine the dq-axis current references. Their main limitation is that they do not consider the saturation effects, but if improved exactness is needed, additional LUTs could be employed.

E. SINGLE CURRENT REGULATOR

This method works at the FW zone based on the regulation of a unique current controller [42], [54], [55], [56]. In deep FW operation, having two current controllers can conflict between them and make the control system unstable when the applied voltage exceeds the maximum available voltage in both transients, and steady-state [54]. The Single Current Regulator (SCR) algorithm switches between two control strategies: one at the LBEMF zone and another at the FW zone (see Fig. 19). The flowchart for transitioning over the base speed is set when the voltage modulus exceeds the maximum allowable value. This maximum voltage depends on the DC voltage and the switching strategy. During the FW operation, the speed closed-loop generates the d-axis current reference, whereas the q-axis voltage is fixed. Nevertheless, the transition under the base speed is done when the d-axis

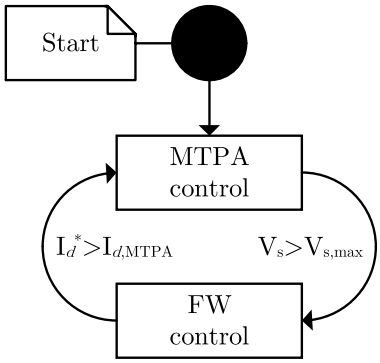

FIGURE 19. Switching strategy for SCR control. Source: [56].

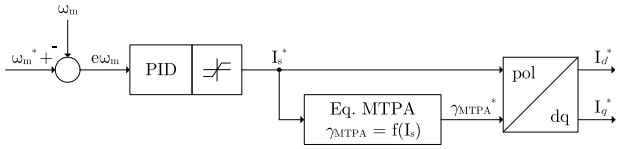

FIGURE 20. Block diagram of the SCR method with MTPA operation. Source: [56].

current is higher than the equivalent d-axis current in the MTPA region.

In the LBEMF zone, this method works in the MTPA region. It controls the d-axis and q-axis currents independently (see Fig. 20). In general, a speed PID controller gives the current modulus setpoint. With the MTPA equation, the d-axis and q-axis current setpoint can be defined. However, this method changes its control algorithm to enter the FW zone when speed increases. Here, the q-axis current controller is removed to uniquely regulate the d-axis current from the speed controller or the torque setpoint, in addition to fixing the q-axis voltage command at a certain value (see Fig. 21). The d-axis current is calculated from the torque setpoint at the output of the speed controller being multiplied by a constant K. The constant value is negative because the demagnetizing current is always opposed to the flux linkage generated by the PMs. The d-axis current command contains both the demagnetizing current and torque information. The full usage of the DC voltage depends on the q-axis voltage value, and the optimal q-axis voltage should be found adaptive to variable speeds and torque.

The main advantage of this method is that there is no conflict between the d-axis and q-axis current controllers during the FW operation. It simplifies the saturation strategy when the current controllers work close to the maximum

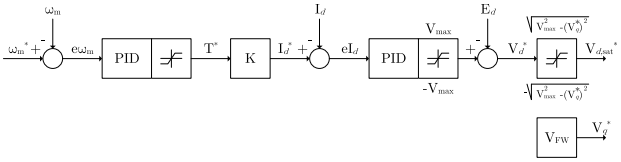

FIGURE 21. Block diagram of the SCR method with FW operation. Source: [42].

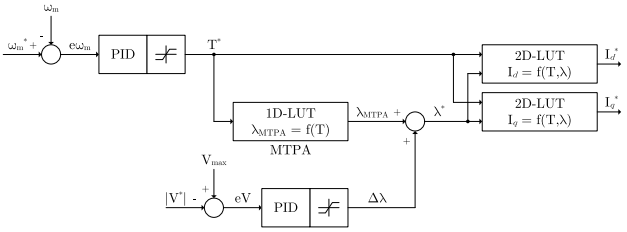

FIGURE 22. Block diagram of the TFC method with LUTs in FW operation with speed reference. Source: [91].

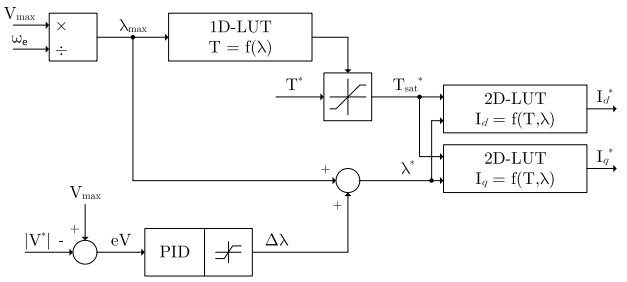

FIGURE 23. Block diagram of the TFC method with LUTs in FW operation with torque reference. Source: [102].

voltage because the q-axis voltage is fixed to a specific value, and the rest of the available voltage will be assigned for the d-axis voltage.

On the contrary, the main disadvantage is the application of analytical switching from low to high speeds and vice versa, making difficult the smooth transition between LBEMF and FW zones [81]. Moreover, the current magnitude limitation cannot be guaranteed since only the d-axis current is directly controlled. Furthermore, this method has weak stability and high sensitivity to the controller parameters [63]. The FW operation is subject to the torque load and the speed command, so to achieve high performance, the q-axis voltage reference should be calculated in real-time according to the speed and d-axis current.

In [42], Zhang et al. claim there is the need for an optimal q-axis voltage criterion for variable speed and load conditions to improve the system's operational efficiency and performance. The authors proposed estimating the q-axis voltage reference according to a 2D-LUT, depending on the mechanical speed and torque setpoint. They claim the DC bus voltage is better utilised, but the phase currents do not seem minor than the original method in the simulation figures during FW operation. Furthermore, they also claim that finding the optimal q-axis reference in terms of variable speed and torque is time-consuming, especially if saturation and cross-saturation effects are to be considered.

In [56], Zhu et al. propose an FW strategy based on SCR and Voltage Angle Control (VAC) to avoid the conflict between the two dq-axis current regulators in deep FW operation. In the FW strategy, the d-axis current controller output is the voltage angle δ. The dq-axis voltage references are calculated according to this angle and the maximum allowable voltage in real-time. They claim the algorithm, which can work at the MTPV region, is not parameter-sensitive, and the DC voltage is thoroughly used by setting the voltage amplitude to its maximum. According to the authors, its main limitation is that the control system can only work as a motor because it will lose control in the generation mode.

F. TORQUE AND FLUX CONTROL METHOD WITH LUTs

The torque and flux control (TFC) with LUTs combines closed-loop control by using the output voltage setpoints from the current PID controllers and the feedforward control with offline tables, unlike DTC, which uses hysteresis controllers and a switching table [87], [88], [89], [90], [91], [92], [93], [94], [95], [96], [97], [98]. According to [96], this methodology reduces the torque and flux ripples compared with the classical DTC scheme. The transition over the base speed is achieved thanks to regulating the voltage modulus by varying the operating flux linkage from the corresponding MTPA value. The dq-axes current setpoints are mapped for the entire flux linkage and torque range.

Fig. 22 and Fig. 23 show the block diagrams of the TFC with LUTs considering the speed or torque setpoints, respectively. This methodology is based on 2D-LUTs to calculate the dq-axis current setpoints from the torque and flux linkage reference values. Furthermore, a third 1D-LUT is used to calculate the base flux linkage regarding the torque setpoint to work in the MTPA region. The maximum allowable flux linkage decreases if the electrical speed rises, and the FW operation is controlled by a feedback path with the magnitude of the applied voltage. $\Delta\lambda$ is the flux reference that the voltage PID controller modifies depending on the maximum voltage.

Similar to the direct open-loop algorithm with the experimental LUTs, this method mainly defines the magnetic saturation through the pre-calculated LUTs. So, the dq-axis current references from the torque and flux setpoints are more accurate, and the machine performance in steady-state is better than other methods that do not consider the magnetic saturation. In [93], Y. Z. Chen et al. present a methodology to get the 2D-LUTs that relate the dq-axis current references to the torque and flux setpoints. Furthermore, the authors claim that an improved voltage control loop is developed to achieve a demand for fast dynamics when the rotor speed increases rapidly by adding an extra stator flux linkage compensation related to the acceleration. A proportional factor multiplying the acceleration of the machine is used to obtain the extra stator flux linkage compensation. However, the authors do not propose a method to calculate this factor.

In [91], Bae et al. enumerate several drawbacks of classical solutions [89]: i) difficult seamless transition between FW operation and Six-Step operation, ii) dynamic torque control, and iii) current harmonics due to Six-Step operation imply the generation of current ripple at the DC-link capacitor of the inverter and reduce its lifetime, degrading the reliability of the driving system. The authors base their affirmation on the fact that most PID current controllers have an anti-windup algorithm to avoid the windup of the integrator. A back-calculation method is usually used, modifying the current reference from the difference between the reference voltage obtained from the current regulators and the output voltage limited by the over modulation. This classical strategy may conflict with the FW controller if both are activated simultaneously. Bae et al. propose removing the anti-windup of the current controllers and separating the feedback control into two independent PID controllers, one for the d-axis voltage and another for the q-axis voltage.

Another shortcoming of classical approaches is the large memory requirement to store the 2D-LUTs and 1D-LUT and the dependence on the previous experimental results of the electric machine. Ekanayake et al. in [98] propose a new algorithm based on the torque-flux plane where the two 2D-LUTs are substituted by two PID controllers that regulate the torque and flux of the machine. The relationships between speed, torque, and flux in different regions are based on curve-fitting techniques instead of LUTs.

G. UNIFIED DIRECT FLUX VECTOR CONTROL IN THE STATOR FLUX FRAME

This method operates in the stator flux coordinates where the d-axis voltage directly controls the stator flux amplitude, while the q-axis current component regulates the torque setpoint. Unlike the other control algorithms based on the rotor frame, this method is based on the stator frame [99], [100]. The load angle (φ) is the phase angle of the stator flux linkage with respect to the rotor flux. A PID regulator that controls the d-axis current from the load angle error sets the transition over the base speed. The angle limit depends on each type of motor. The exact value depends on the motor and can be evaluated by model manipulation or by dedicated tests at no load with trial-and-error values in the particular range [100].

The control algorithm requires three different PID controllers: two of them are needed to control the flux linkage magnitude, and q-axis current, respectively, and one more is necessary for the load angle limitation at high speeds [100]. Fig. 24 depicts the control block diagram. A flux observer calculates the estimated flux linkage and the load angle from the $\alpha\beta$-axis voltage and current magnitudes. The optimization algorithm determines the stator flux linkage and the q-axis current considering the torque, MTPA, and MTPV equations.

The main advantage is that the method is compatible with all AC machines: IMs, PMSMs, and SyRMs [100]. Moreover, this method combines the benefits of the direct flux control and uses only one current regulation channel for the torque

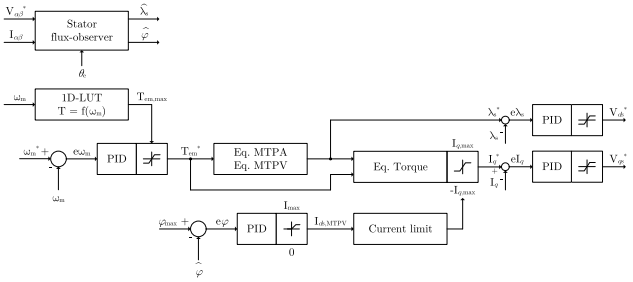

FIGURE 24. Block diagram of the UDFVC method. Source: [100].

setpoint. So, the FW operation and the current limit are straightforward to accomplish.

The main shortcoming is the need for a flux observer that depends on the machine parameters. Then, any mismatch between the actual parameters and their estimated values can lead to a flux estimation error in the low-speed region and a possible steady-state torque estimation error. Besides, the maximum load angle must be determined experimentally, which makes the method dependable on the machine and the bench test [81].

H. VECTOR CURRENT CONTROL

The Vector Current Control (VCC) method achieve the transition over the base speed by applying a variation on the d-axis current, q-axis current or the current angle, which is calculated in the MTPA zone, from the voltage magnitude error [43], [46], [58], [59], [60], [61], [63], [65], [66], [67], [68], [69], [70], [71], [74], [76], [77], [78], [79], [80], [81], [82], [83], [84], [85], [86], voltage error [72], [75], [103], current error [57], and duty cycles error [62], [64], [73].

The most common strategy for industrial applications is the regulation of the voltage magnitude [56], [81]. Generally, there are no voltage sensors at the output of the power converter, and the feedback path of the voltage vector results from the output of the current PID controllers. Hence, this method neglects several effects, such as the voltage drop of the power switches, the dead time or the signal conditioning delays, although some authors claim to compensate them [81].

Fig. 25 depicts the block diagrams that correspond to the different VCC methods studied in the literature. In terms of comparison, in the case of regulating the voltage error or duty cycles, the use of low-pass filters in the control loop impacts the dynamic control performance. Besides, the strategies to regulate the voltage error and the duty cycles are based on the overmodulation capabilities of the power converter and on enabling the increase of the maximum available voltage at the expense of additional current harmonics [81].

1) Regulation on the voltage magnitude

This method regulates the voltage norm based on a feedback voltage control loop. This loop compares the voltage vector setpoint, which is generated by the current PID controllers, with the voltage limit. If the norm value is higher than

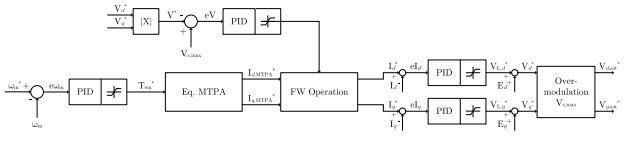

(a) Regulation on the voltage magnitude.

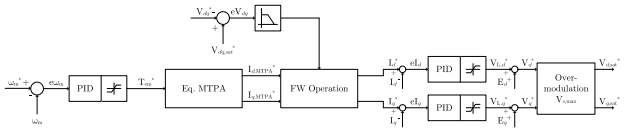

(b) Regulation on the voltage error.

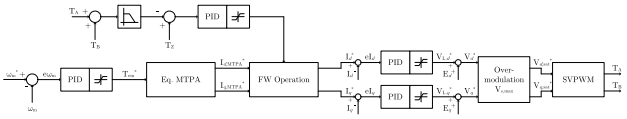

(c) Regulation on the duty cycles.

FIGURE 25. Block diagram of different VCC methods.

the imposed limit, the chosen FW variable is modified to reduce the flux of the stator windings by controlling the current vector. The voltage controller can be synthesized by a cascaded method using the closed-loop model of the current regulation and positioning the FW bandwidth accordingly. In the case of an external speed control loop, the FW regulation dynamic should be negligible according to the mechanical dynamics [81]. Fig. 26 depicts the three different strategies proposed in the literature to select the FW variable control: d-axis current, q-axis current, or γ current angle. The comparison between the three control structures is detailed in Section IV.

The main advantage of this strategy is that the saturation effects and the resistor voltage drop parameters are considered when transitioning between the LBEMF and FW zones thanks to the feedback path without knowing the exact value of these parameters.

The main drawback of this method is the voltage limit to start the FW operation because this value affects the power density of the powertrain. The limit voltage is defined as a partial quantity of the maximum voltage applied to the electric machine to avoid low current regulator dynamics and possible instability required for load transients and low-frequency disturbances. The current PID controllers are generally saturated to the maximum available voltage. Although working in the overmodulation region or using the Six-Step switching strategy would help to improve the employment of the DC voltage, it will imply the increase of the torque ripple, the reduction of control dynamics, and the injection of current harmonics, which will favour the appearance of noise and vibrations. Another disadvantage is the non-linear relationship between the voltage magnitude and the variable to control, making it challenging to tune the FW controller for a wide bandwidth of working points. Besides, the static gain of the closed-loop plant is not constant in all speed ranges, as it modifies the control effort for the same input variation [43], [83].

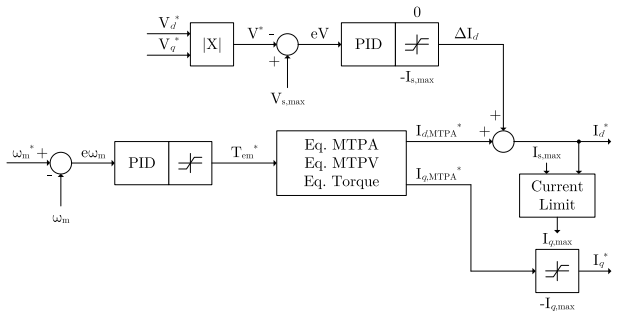

(a) I_d control.

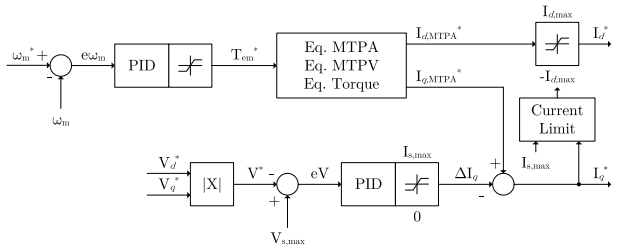

(b) I_q control.

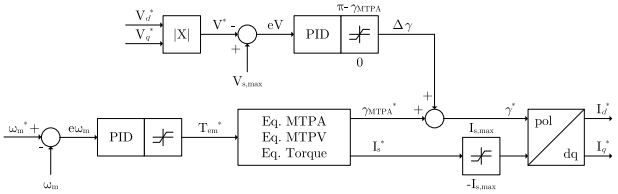

(c) γ control.

FIGURE 26. Block diagram of the VCC method regulating the voltage magnitude.

Bolognani et al. in [43] propose a voltage regulator with an adaptive gain. The authors suggest an extensive speed range where the plant is stable and has a higher torque versus speed powertrain performance. Besides, they made a static and dynamic analytical investigation of the feedback voltage control loop according to the three different strategies shown in Fig. 26. The main conclusion is that the strategy that varies the current angle provides a smoother transition in the entire FW zone.

In [81], Sepulchre et al. claim to have developed an FW algorithm that is capable of working in the MTPV region, and it smoothly changes from the LBEMF to the FW zone without switching algorithms. It is done by adjusting the d-axis current in the FW operation. The authors considered the maximum power of the battery that mainly affects the constant power region. Although the authors claimed that simulation and experimental results are satisfactorily concordant, it is shown that there are discrepancies between the dq-axis trajectories, mainly when the electric machine enters the MTPV zone.

Lee et al. in [68] analyse the performance of the FW strategy during the overmodulation area, with modulation strategies other than SVPWM. This article analyses the consequences of the error committed during the overmodulation

TABLE 3. Comparison of control strategies for FW operation.

Control strategies	Advantages	Drawbacks	References
Analytical direct calculation	– Good stability. – Good transient response.	– Susceptible to the machine parameters, the variation of these parameters with temperature or saturation effects, and operating conditions. – Excessive calculation time for IPMSM implementation. – Resistor drop and saturation effect are not considered. – MTPV is not considered.	[20], [21], [45], [47]–[51]
Direct open-loop algorithm with experimental LUTs	– Consideration of inductance variation due to magnetic saturation. – Torque reference is correctly followed independently of the degree of saturation.	– Sizeable experimental setup to obtain the different LUTs in all the torque-speed range	[52], [53]
SCR	– No conflict between the dq-axis current controllers during FW operation.	– Lumpy transition between the LBEMF and FW operation. – The current magnitude is not limited. – Weak stability and high sensitivity to the controller parameters. – q-axis voltage reference depends on the load and the speed reference to achieve a good performance.	[42], [54]–[56]
TFC method with LUT	– Definition of the magnetic saturation. – Robustness to the variation of the motor parameters and uncertainties.	– Large memory usage in order to store the LUTs. – Complex implementation to manage some out-of-domain operating conditions. – An extensive off-line measurement and post-processing efforts should be carried out to fill in the tables.	[87]–[98]
UDFVC in the stator flux frame	– Compatible with all AC machines. – Direct-flux control and a unique current controller to manage the torque setpoint.	– Requirement of a flux observer that is dependent on the machine. – The maximum load torque should be determined experimentally. – No MTPV considered.	[99], [100]
VCC on voltage magnitude	– Consideration of the resistor voltage drop and the saturation effects in the transition to/from the FW operation.	– Limitation of the maximum utilization of the DC bus voltage. – Inaccuracies because of errors between the predicted magnitude of the voltage and the actual voltage applied to the machine.	[43], [46], [58]–[61], [63], [65]–[71], [74], [76]–[86]
VCC on voltage error	– Over-modulation strategy enables the increase of the maximum voltage available.	– Low control dynamic performance due to LPFs. – Injection of additional current harmonics.	[72], [75], [103]
VCC on current error		– Low control dynamic performance due to LPFs.	[57]
VCC on duty error	– Over-modulation strategy enables the increase of the maximum voltage available.	– Low control dynamic performance due to LPFs. – Injection of additional current harmonics.	[62], [64], [73]

area between the voltage vector on the feedback path and the voltage applied to the electric machine. Besides, the authors proposed a method to minimise the calculated voltage while performing FW control to reach high speeds with the minimum current. Nevertheless, the main limitation of the analytical study is its only application for SPMSMs, and the saturation effects and the resistor voltage drop were not considered.

IV. DISCUSSION

The rapid penetration of EVs in the automotive sector makes it mandatory to improve the efficiency in the energy flow of powertrains to extend the battery life and achieve compact designs. In this article, the main focus is on the torque and speed control algorithm to get the maximum performance of the electric machine in all the speed ranges. Special mention is made to the deep FW operation to reach the maximum torque at high speeds, which is required for electric traction machines.

The most common electric machine used in the electric powertrain is a PMSM, specifically an IPMSM, due to several reasons: i) high power density and high torque to current ratio; ii) high torque at low speed; iii) high efficiency; iv) reduced size; v) precise control at low speed; vi) high flux-weakening capability. Nevertheless, the selection of the electric machine is an arguable topic, and the newer topologies will address the issue from three points of view: design, manufacturing, and life cycle assessment. The main goal of new concepts is to reduce the use of rare resources with alternative materials or advanced configurations while achieving lower cost, higher efficiency, and power density than the current electric machines in the market.

The characteristic curves of a PMSM depend only on its intrinsic features. Once these features are extracted, the power converter should achieve the best efficiency in all the speed ranges. A debatable topic in the literature is the variation of the characteristic parameters with the current and the temperature. Several authors studied the dependence of the dq-axis inductances regarding the current distribution and the flux linkage and resistance regarding the temperature. Other authors have included this variation in the control algorithm to achieve the maximum performance of the

TABLE 4. Comparison of different VCC methods regulating on the voltage magnitude analysed in the literature.

Reference	Output Voltage Controller	MTPV	Inductance Saturation	Reference System	Coordinate System	Voltage Loop Analysis	Reference Signal	Machine
[58]	d-axis current			Natural	Cartesian		Speed	IPMSM
[59]	current angle		*	Natural	Polar		Torque	IPMSM
[60]	d-axis current		*	Per-unit	Cartesian	*	Speed	IPMSM
[70]	d-axis current	*		Natural	Cartesian		Speed	IPMSM
[61]	current angle			Natural	Polar	*	Speed	IPMSM
[71]	dq-axis current	*		Natural	Cartesian		Speed	SPMSM
[63]	current angle			Natural	Polar	*	Speed	SPMSM
[43]	current angle			Natural	Polar	*	Speed	IPMSM
[46]	d-axis current	*		Natural	Cartesian		Torque	IPMSM
[77]	d-axis current	*		Natural	Cartesian		Speed	IPMSM
[65]	d-axis current			Natural	Cartesian	*	Speed	IPMSM
[78]	current angle	*		Natural	Polar		Speed	SyRM
[79]	d-axis current	*	*	Natural	Cartesian		Speed	IPMSM
[74]	d-axis current	*		Natural	Cartesian		Speed	IPMSM
[76]	d-axis current	*		Natural	Cartesian		Speed	IPMSM
[81]	d-axis current	*		Natural	Cartesian		Torque	IPMSM
[82]	d-axis current	*		Natural	Cartesian		Torque	IPMSM
[80]	d-axis current	*		Natural	Cartesian		Torque	IPMSM
[66]	current angle			Natural	Polar		Speed	IPMSM
[67]	d-axis current			Natural	Cartesian		Speed	IPMSM
[83]	current angle	*	*	Per-unit	Polar	*	Speed	SyRM
[84]	current angle	*		Per-unit	Polar		Torque/Speed	IPMSM
[85]	d-axis current	*		Natural	Cartesian		Speed	IPMSM
[86]	current angle	*	*	Per-unit	Polar		Torque/Speed	IPMSM
[68]	d-axis current			Natural	Cartesian		Torque	SPMSM
[69]	current angle		*	Natural	Polar		Torque (braking)	IPMSM

electric machine. Table 3 summarises the main characteristics, advantages and drawbacks of the FW strategies studied in Section III.

As discussed in Section III, the VCC method is the most common choice to work in the FW zone. Different techniques have been examined in the literature. Table 4 shows the main characteristics of each one: output voltage regulator (d-axis current variation, q-axis current variation or current angle variation), MTPV implementation, reference system (natural or per-unit), coordinate system (Cartesian or polar), voltage loop analysis, reference signal (torque, speed or both), and electric machine (IPMSM, SPMSM, or SyRM).

The authors suggest the best solution for VCC control strategies is to consider the output of the voltage regulator as the current angle instead of the d-axis current or q-axis current, and it will maximise the dynamic performance of the controller [43]. Then, a lower voltage margin can be considered, and high torque and efficiency are achieved, increasing the actual power density of the electric drive. The authors implemented an FW algorithm with torque reference and the speed limit in a unified scheme, using a per-unit system to be executed effectively in a low-level and low-cost microcontroller, therefore achieving a smooth transition among all possible trajectories [84]. Furthermore, in the case of having the variation of the dq-axis inductances regarding the dq-axis current, either by numerical simulations or by experimental results, the authors propose to include them through 2D-LUTs in the torque, MTPA, and MTPV equations [86].

The authors propose investigating newer control strategies by analyzing the optimization problem of reduced losses in the entire powertrain. It means not only achieving the best performance of the electric machine but also the power electronics working in the best efficiency point of the integral solution [14].

V. CONCLUSION

Although the development of new electric machines without the dependency on rare-earth materials has gained interest in the past few years, the common choice as the primary traction component in EV applications is a PMSM. EV manufacturers still prefer the PMSM option due to its high efficiency, superior power and torque density, and wide speed range at constant power. IPMSMs are generally utilised rather than SPMSMs due to a higher torque and power per volume ratio obtained from the additional reluctant torque.

At speeds lower than the nominal value, the MTPA strategy is the most commonly used to achieve the best performance of the machine in traction applications. Over the nominal speed, an FW strategy should be applied to widen the speed region at constant power and get the maximum torque in all the speed range. This article has reviewed the main characteristics and the diagram blocks of several control strategies that work in the FW zone presented in the literature. The findings of this research can be summarised as follows:

- **Robustness to parameter modification and model unsureness**: VCC strategies inherently consider the resistor voltage drop and the saturation effects in the transition to/from the FW operation. The saturation effects at high speeds and high currents can be considered through LUTs as it is done for the feedforward approaches.
- **Computational complexity**: Feedforward methods require knowing about the machine parameters such as

the resistance and inductance. Hence, a lot of effort must be made to parametrise the electric machine through FEA or experimental tests. Including all these results require a great deal of memory and computational effort.

- **Dynamic response and control stability**: Feedforward strategies have fast responses due to the lack of closed-loop structures. However, VCC control strategies easily obtain stability, robustness and good performance in the transition between the LBEMF and FW zones.

Methods based on VCC strategies that regulate the modulus of the applied voltage are the most commonly used in the bibliography due to a relatively more straightforward structure. These techniques can be easily implemented inside standard vector controller drives without the dependency of extensive knowledge of the parameters of the electric machine. In the literature, there are three different implementations of VCC strategies referring to the variable that is changed during the FW operation: i) d-axis current, ii) q-axis current, and iii) angle of the current. Among them, the solution that considers the output of the voltage regulator as the angle of the current maximises the dynamic performance. So, a lower voltage margin should be considered, and high torque and efficiency are achieved.

Even so, there are several issues to be dealt with and tackled in the following years.

- As SyRMs are gaining penetration in the EV market due to their non-dependency on rare-earth materials, it seems mandatory to **adapt** the **FW algorithm to control both PMSMs and SyRMs** in all the torque-speed range, considering the LBEMF zone at low-speeds and the FW zone at high speeds.
- A **control strategy** should be developed in order to **maximise** the **efficiency of the electric powertrain as a whole**, including the power source, the power electronics and the electric machines. This approach will get the maximum performance of the entire system with the main objective to increase the vehicle's mileage and extend the battery's lifetime.
- **Fault-tolerant FW algorithms** need to be developed to handle sudden failures at high speeds to protect both the electric machine and power electronics.

This analysis should contribute to future investigations in this field to adapt these FW control algorithms to different electric machines and get the maximum performance of the powertrain during traction and braking control.

REFERENCES

[1] *Inventory of U.S. Greenhouse Gas Emissions and Sinks: 1990–2015*, United States Environ. Protection Agency, Washington, DC, USA, 2017.

[2] S. Wang and M. Ge. (Oct. 2019). *Everything You Need to Know About the Fastest-Growing Source of Global Emissions: Transport*. [Online]. Available: https://www.wri.org/blog/2019/10/everything-you-need-know-about-fastest-growing-source-global-emissions-transport

[3] B. Bilgin, P. Magne, P. Malysz, Y. Yang, V. Pantelic, M. Preindl, A. Korobkine, W. Jiang, M. Lawford, and A. Emadi, "Making the case for electrified transportation," *IEEE Trans. Transport. Electrific.*, vol. 1, no. 1, pp. 4–17, Jun. 2015, doi: 10.1109/TTE.2015.2437338.

[4] I. López, E. Ibarra, A. Matallana, J. Andreu, and I. Kortabarria, "Next generation electric drives for HEV/EV propulsion systems: Technology, trends and challenges," *Renew. Sustain. Energy Rev.*, vol. 114, pp. 1–23, Oct. 2019, doi: 10.1016/j.rser.2019.109336.

[5] A. Karki, S. Phuyal, D. Tuladhar, S. Basnet, and B. P. Shrestha, "Status of pure electric vehicle power train technology and future prospects," *Appl. Syst. Innov.*, vol. 3, no. 35, pp. 1–28, Aug. 2020, doi: 10.3390/asi3030035.

[6] A. A. Abdelhafez, M. A. Aldalbehi, N. F. Aldalbehi, F. R. Alotaibi, N. A. Alotaibi, and R. S. Alotaibi, "Comparative study for machine candidates for high speed traction applications," *Int. J. Electr. Eng.*, vol. 10, no. 1, pp. 71–84, 2017.

[7] T. Finken, M. Felden, and K. Hameyer, "Comparison and design of different electrical machine types regarding their applicability in hybrid electrical vehicles," in *Proc. 18th Int. Conf. Electr. Mach.*, Sep. 2008, pp. 1–5, doi: 10.1109/ICELMACH.2008.4800044.

[8] A. M. Bazzi, "Electric machines and energy storage technologies in EVs and HEVs for over a century," in *Proc. Int. Electr. Mach. Drives Conf.*, May 2013, pp. 212–219, doi: 10.1109/IEMDC.2013.6556255.

[9] Z. Q. Zhu, W. Q. Chu, and Y. Guan, "Quantitative comparison of electromagnetic performance of electrical machines for HEVs/EVs," *CES Trans. Electr. Mach. Syst.*, vol. 1, no. 1, pp. 37–47, 2020, doi: 10.23919/tems.2017.7911107.

[10] R. Krishnan, *Permanent Magnet Synchronous and Brushless DC Motor Drives*. Blacksburg, VA, USA: CRC Press, 2010.

[11] YASA. (Jan. 2023). *YASA Motors*. [Online]. Available: https://www.yasa.com/

[12] H. C. Idoko, U. B. Akuru, R. J. Wang, and O. Popoola, "Potentials of brushless stator-mounted machines in electric vehicle drives—A literature review," *World Electr. Veh. J.*, vol. 13, no. 5, p. 26, May 2022, doi: 10.3390/wevj13050093.

[13] J. Edmondson, D. Wyatt, and L. Gear, "Electric motors for electric vehicles 2022–2032 (sample pages)," IDTechEx, Cambridge, U.K., Tech. Rep., 2022.

[14] H. Hammerer, G. Wilhelm, M. Ivarson, F. Duchi, and P. Winzer, "AVL digital tech day: The inverter key to success," AVL, Graz, Austria, Tech. Rep., 2021.

[15] Silicon Mobility. (Dec. 2019). *Increasing the Range of EV With the Same Battery—Part II—More Efficiency With Better Software*. [Online]. Available: https://www.silicon-mobility.com/increasing-the-range-of-ev-with-the-same-battery-part-ii-more-efficiency-with-better-software/

[16] J.-H. Park, W. Jo, E.-T. Jeon, S.-H. Kim, C.-H. Lee, J.-H. Lee, J.-H. Lee, J. Yi, and C.-Y. Won, "Variable switching frequency control-based six-step operation method of a traction inverter for driving an interior permanent magnet synchronous motor for a railroad car," *IEEE Access*, vol. 10, pp. 33829–33843, 2022, doi: 10.1109/ACCESS.2022.3162877.

[17] D. Gerada, A. Mebarki, N. L. Brown, C. Gerada, A. Cavagnino, and A. Boglietti, "High-speed electrical machines: Technologies, trends, and developments," *IEEE Trans. Ind. Electron.*, vol. 61, no. 6, pp. 2946–2959, Jun. 2014, doi: 10.1109/TIE.2013.2286777.

[18] L. Chédot and G. Friedrich, "A cross saturation model for interior permanent magnet synchronous machine. Application to a starter-generator," in *Proc. Conf. Rec. IEEE Ind. Appl. Conf., 39th IAS Annu. Meeting.*, Oct. 2004, pp. 64–70, doi: 10.1109/IAS.2004.1348389.

[19] L. Nguyen and T. C. Pham, "Optimal tracking control for PMSM with partially unknown dynamics, saturation voltages, torque, and voltage disturbances," *IEEE Trans. Ind. Electron.*, vol. 69, no. 4, pp. 3481–3491, Apr. 2022, doi: 10.1109/TIE.2021.3075892.

[20] N. V. Olarescu, M. Weinmann, S. Zeh, and S. Musuroi, "Novel flux weakening control algorithm for PMSMS," in *Proc. Int. Conf. Power Eng., Energy Electr. Drives*, Mar. 2009, pp. 123–127, doi: 10.1109/POWERENG.2009.4915216.

[21] A. Sanz, E. Oyarbide, R. Gálvez, C. Bernal, P. Molina, and I. S. Vicente, "Analytical maximum torque per volt control strategy of an interior permanent magnet synchronous motor with very low battery voltage," *IET Electr. Power Appl.*, vol. 13, no. 7, pp. 1042–1050, Jul. 2019, doi: 10.1049/iet-epa.2018.5469.

[22] D. Lu and N. C. Kar, "A review of flux-weakening control in permanent magnet synchronous machines," in *Proc. IEEE Vehicle Power Propuls. Conf.*, Sep. 2010, pp. 1–6, doi: 10.1109/VPPC.2010.5728986.

[23] M. Meyer, T. Grote, and J. Bocker, "Direct torque control for interior permanent magnet synchronous motors with respect to optimal efficiency," in *Proc. Eur. Conf. Power Electron. Appl.*, 2007, pp. 1–9, doi: 10.1109/EPE.2007.4417370.

[24] S. M. S. I. Shakib, D. Xiao, R. Dutta, K. S. Alam, I. Osman, M. F. Rahman, and M. P. Akter, "An analytical approach to direct torque and flux control of interior permanent magnet synchronous machine for deep field weakening without using pre-calculated lookup tables," in *Proc. 10th Int. Conf. Power Electron. ECCE Asia (ICPE - ECCE Asia)*, May 2019, pp. 1–6.

[25] Y. Inoue, S. Morimoto, and M. Sanada, "Comparative study of PMSM drive systems based on current control and direct torque control in flux-weakening control region," *IEEE Trans. Ind. Appl.*, vol. 48, no. 6, pp. 2382–2389, Nov./Dec. 2012, doi: 10.1109/TIA.2012.2227134.

[26] X. D. T. Garcia, B. Zigmund, A. A. Terlizzi, R. Pavlanin, and L. Salvatore, "Comparison between FOC and DTC strategies for permanent magnet synchronous motors," *Adv. Electr. Electron. Eng.*, vol. 5, no. 1, pp. 76–81, 2006.

[27] R. Bojoi, M. Pastorelli, J. Bottomley, P. Giangrande, and C. Gerada, "Sensorless control of PM motor drives—A technology status review," in *Proc. IEEE Workshop Electr. Mach. Design, Control Diagnosis (WEMDCD)*, Mar. 2013, pp. 168–182, doi: 10.1109/WEMDCD.2013.6525177.

[28] F. G. Capponi, G. De Donato, L. Del Ferraro, O. Honorati, M. C. Harke, and R. D. Lorenz, "AC brushless drive with low-resolution Hall-effect sensors for surface-mounted PM machines," *IEEE Trans. Ind. Appl.*, vol. 42, no. 2, pp. 526–535, Mar. 2006, doi: 10.1109/TIA.2005.863904.

[29] L. Yu, Y. Zhang, and W. Huang, "Accurate and efficient torque control of an interior permanent magnet synchronous motor in electric vehicles based on Hall-effect sensors," *Energies*, vol. 10, no. 3, pp. 1–16, Mar. 2017, doi: 10.3390/en10030410.

[30] S. Y. Kim, C. Choi, K. Lee, and W. Lee, "An improved rotor position estimation with vector-tracking observer in PMSM drives with low-resolution Hall-effect sensors," *IEEE Trans. Ind. Electron.*, vol. 58, no. 9, pp. 4078–4086, Sep. 2011, doi: 10.1109/TIE.2010.2098367.

[31] J. A. Cortajarena, S. García, J. Cortajarena, O. Barambones, and P. Alkorta, "Influence of the rotor angle precision in control of interior permanent magnet synchronous machine drives and improvement method using sensorless estimator with Hall sensors," *IET Power Electron.*, vol. 12, no. 3, pp. 383–391, Jan. 2019, doi: 10.1049/ietpel.2018.5143.

[32] S. Morimoto, M. Sanada, and Y. Takeda, "Sinusoidal current drive system of permanent magnet synchronous motor with low resolution position sensor," in *Proc. Conf. Rec. IEEE Ind. Appl. Conf. 31st IAS Annu. Meeting (IAS)*, vol. 1, Oct. 1996, pp. 9–14, doi: 10.1109/IAS.1996.556990.

[33] S. B. Ozturk, B. Akin, H. A. Toliyat, and F. Ashrafzadeh, "Low-cost direct torque control of permanent magnet synchronous motor using Hall-effect sensors," in *Proc. 21st Annu. IEEE Appl. Power Electron. Conf. Expo. (APEC)*, Mar. 2006, pp. 667–673, doi: 10.1109/APEC.2006.1620610.

[34] X. Zhang and W. Zhang, "An improved rotor position estimation in PMSM with low-resolution Hall-effect sensors," in *Proc. 17th Int. Conf. Electr. Mach. Syst. (ICEMS)*, Oct. 2014, pp. 2722–2727, doi: 10.1109/ICEMS.2014.7013961.

[35] L. Kreindler, I. Iacob, G. Casaru, A. Sarca, R. Olteanu, and D. Matianu, "PMSM drive using digital Hall position sensors for light EV applications," in *Proc. 9th Int. Symp. Adv. Topics Electr. Eng. (ATEE)*, May 2015, pp. 199–204, doi: 10.1109/ATEE.2015.7133764.

[36] H. Mehta, V. Joshi, U. Thakar, M. Kuber, and P. Kurulkar, "Speed control of PMSM with Hall sensors using DSP TMS320F2812," in *Proc. IEEE 11th Int. Conf. Power Electron. Drive Syst.*, Jun. 2015, pp. 295–300, doi: 10.1109/PEDS.2015.7203482.

[37] A. Yoo, S. Sul, D. Lee, and C. Jun, "Novel speed and rotor position estimation strategy using a dual observer for low-resolution position sensors," *IEEE Trans. Power Electron.*, vol. 24, no. 12, pp. 2897–2906, Dec. 2009, doi: 10.1109/TPEL.2009.2022969.

[38] Z. Wang, K. Wang, J. Zhang, C. Liu, and R. Cao, "Improved rotor position estimation for permanent magnet synchronous machines based on Hall-effect sensors," in *Proc. IEEE Int. Conf. Aircr. Utility Syst.*, Oct. 2016, pp. 911–916.

[39] Y. Zhao, W. Huang, J. Yang, F. Bu, and S. Liu, "A PMSM rotor position estimation with low-cost Hall-effect sensors using improved PLL," in *Proc. IEEE Transp. Electrific. Conf. Expo, Asia–Pacific (ITEC Asia–Pacific)*, Jun. 2016, pp. 804–807, doi: 10.1109/ITEC-AP.2016.7513058.

[40] G. Liu, B. Chen, and X. Song, "High-precision speed and position estimation based on Hall vector frequency tracking for PMSM with bipolar Hall-effect sensors," *IEEE Sensors J.*, vol. 19, no. 6, pp. 2347–2355, Mar. 2019, doi: 10.1109/JSEN.2018.2885020.

[41] C. Miguel-Espinar, D. Heredero-Peris, G. Igor-Gross, M. Llonch-Masachs, and D. Montesinos-Miracle, "An enhanced electrical angle representation in PMSM control with misplaced Hall-effect switch sensors," in *Proc. 23rd Int. Conf. Electr. Mach. Syst. (ICEMS)*, Nov. 2020, pp. 1454–1459, doi: 10.23919/ICEMS50442.2020.9291194.

[42] Y. Zhang, L. Xu, M. K. Güven, S. Chi, and M. Illindala, "Experimental verification of deep field weakening operation of a 50-kW IPM machine by using single current regulator," *IEEE Trans. Ind. Appl.*, vol. 47, no. 1, pp. 128–133, Jan. 2011, doi: 10.1109/TIA.2010.2091478.

[43] S. Bolognani, S. Calligaro, and R. Petrella, "Adaptive flux-weakening controller for interior permanent magnet synchronous motor drives," *IEEE J. Emerg. Sel. Topics Power Electron.*, vol. 2, no. 2, pp. 236–248, Jun. 2014, doi: 10.1109/JESTPE.2014.2299153.

[44] J. Wang, J. Wu, C. Gan, and Q. Sun, "Comparative study of flux-weakening control methods for PMSM drive over wide speed range," in *Proc. 19th Int. Conf. Electr. Mach. Syst.*, 2016, pp. 1–6.

[45] M. Tursini, E. Chiricozzi, and R. Petrella, "Feedforward flux-weakening control of surface-mounted permanent-magnet synchronous motors accounting for resistive voltage drop," *IEEE Trans. Ind. Electron.*, vol. 57, no. 1, pp. 440–448, Jan. 2010, doi: 10.1109/TIE.2009.2034281.

[46] L. Sepulchre, M. Fadel, M. Pietrzak-David, and G. Porte, "Flux-weakening strategy for high speed PMSM for vehicle application," in *Proc. Int. Conf. Electr. Syst. Aircr., Railway, Ship Propuls. Road Vehicles Int. Transp. Electrif. Conf.*, 2016, pp. 1–7, doi: 10.1109/ESARS-ITEC.2016.7841413.

[47] Z. Fangyang, R. Feng, L. Jianjun, and H. Peng, "Study on flux-weakening control for PMSM," in *Proc. 4th Int. Symp. Knowl. Acquisition Modeling*, Oct. 2011, pp. 192–195, doi: 10.1109/KAM.2011.58.

[48] S. Morimoto, M. Sanada, and Y. Takeda, "Wide-speed operation of interior permanent magnet synchronous motors with high-performance current regulator," *IEEE Trans. Ind. Appl.*, vol. 30, no. 4, pp. 920–926, Jul./Aug. 1994, doi: 10.1109/28.297908.

[49] S. Ekanayake, R. Dutta, M. F. Rahman, and D. Xiao, "Deep flux weakening control of a segmented interior permanent magnet synchronous motor with maximum torque per voltage control," in *Proc. 41st Annu. Conf. IEEE Ind. Electron. Soc. (IECON)*, Nov. 2015, pp. 4802–4807, doi: 10.1109/IECON.2015.7392851.

[50] S. Ekanayake, A. Pouramin, R. Dutta, and M. F. Rahman, "Verification of a novel voltage control strategy for MTPV control of a fractional-slot concentrated-winding IPMSM," in *Proc. IEEE Int. Electr. Mach. Drives Conf. (IEMDC)*, May 2017, pp. 1–6, doi: 10.1109/IEMDC.2017.8001867.

[51] S. Wang, J. Kang, M. Degano, A. Galassini, and C. Gerada, "An accurate wide-speed range control method of IPMSM considering resistive voltage drop and magnetic saturation," *IEEE Trans. Ind. Electron.*, vol. 67, no. 4, pp. 2630–2641, Apr. 2020, doi: 10.1109/TIE.2019.2912766.

[52] M. Meyer and J. Bocker, "Optimum control for interior permanent magnet synchronous motors (IPMSM) in constant torque and flux weakening range," in *Proc. 12th Int. Power Electron. Motion Control Conf.*, Aug. 2006, pp. 282–286, doi: 10.1109/EPEPEMC.2006.4778413.

[53] M. S. Kunter, T. Schoenen, W. Hoffmann, and R. W. De Doncker, "IPMSM control regime for a hybrid-electric vehicle application," in *Proc. Emobility Electr. Power Train*, Nov. 2010, pp. 1–5, doi: 10.1109/EMOBILITY.2010.5668054.

[54] L. Xu, Y. Zhang, and M. K. Guven, "A new method to optimize *Q*-axis voltage for deep flux weakening control of IPM machines based on single current regulator," in *Proc. Int. Conf. Electr. Mach. Syst.*, 2008, pp. 2750–2754.

[55] T. Hu, F. Lin, L. Cui, Q. Yuan, and Z. Yang, "The flux-weakening control of interior permanent magnet synchronous traction motors for high-speed train," in *Proc. 1st Int. Work. High-Speed Intercity Railway*, vol. 1, 2012, pp. 451–461.

[56] L. Zhu, S. Xue, X. Wen, Y. Li, and L. Kong, "A new deep field-weakening strategy of IPM machines based on single current regulator and voltage angle control," in *Proc. IEEE Energy Convers. Congr. Expo.*, Sep. 2010, pp. 1144–1149, doi: 10.1109/ECCE.2010.5617844.

[57] S. D. Sudhoff, K. A. Corzine, and H. J. Hegner, "A flux-weakening strategy for current-regulated surface-mounted permanent-magnet machine drives," *IEEE Trans. Energy Convers.*, vol. 10, no. 3, pp. 431–437, Sep. 1995, doi: 10.1109/60.464865.

[58] J.-M. Kim and S.-K. Sul, "Speed control of interior permanent magnet synchronous motor drive for the flux weakening operation," *IEEE Trans. Ind. Appl.*, vol. 33, no. 1, pp. 43–48, Jan. 1997, doi: 10.1109/28.567075.

[59] J. Wai and T. M. Jahns, "A new control technique for achieving wide constant power speed operation with an interior PM alternator machine," in *Proc. Conf. Rec. IEEE Ind. Appl. Conf. 36th IAS Annu. Meeting*, Sep./Oct. 2001, pp. 807–814, doi: 10.1109/IAS.2001.955545.

[60] N. Bianchi, S. Bolognani, and M. Zigliotto, "High-performance PM synchronous motor drive for an electrical scooter," *IEEE Trans. Ind. Appl.*, vol. 37, no. 5, pp. 1348–1355, Sep./Oct. 2001, doi: 10.1109/28.952510.

[61] S. Bolognani, S. Calligaro, and R. Petrella, "Optimal voltage feedback flux-weakening control of IPMSM," in *Proc. 37th Annu. Conf. IEEE Ind. Electron. Soc. (IECON)*, Nov. 2011, pp. 4170–4175, doi: 10.1109/IECON.2011.6119770.

[62] P.-Y. Lin and Y.-S. Lai, "Voltage control technique for the extension of DC-link voltage utilization of finite-speed SPMSM drives," *IEEE Trans. Ind. Electron.*, vol. 59, no. 9, pp. 3392–3402, Sep. 2012, doi: 10.1109/TIE.2011.2173095.

[63] F. Gao, S. Bozhko, Y. S. Shen, and G. Asher, "Control design for PMM starter-generator operated in flux-weakening mode," in *Proc. 48th Int. Univ. Power Eng. Conf. (UPEC)*, Sep. 2013, pp. 1–6, doi: 10.1109/UPEC.2013.6714982.

[64] . Li, Q. Wang, J. Yu, and J. Xiong, "Field-weakening control algorithm for interior permanent magnet synchronous motor based on space-vector modulation technique," *J. Converg. Inf. Technol.*, vol. 8, no. 3, pp. 167–175, Feb. 2013.

[65] S. Bozhko, M. Rashed, C. I. Hill, S. S. Yeoh, and T. Yang, "Flux-weakening control of electric starter–generator based on permanent-magnet machine," *IEEE Trans. Transport. Electrific.*, vol. 3, no. 4, pp. 864–877, Dec. 2017, doi: 10.1109/TTE.2017.2718221.

[66] T. Deng, Z. Su, J. Li, P. Tang, X. Chen, and P. Liu, "Advanced angle field weakening control strategy of permanent magnet synchronous motor," *IEEE Trans. Veh. Technol.*, vol. 68, no. 4, pp. 3424–3435, Apr. 2019, doi: 10.1109/TVT.2019.2901275.

[67] D. Ding, G. Wang, N. Zhao, G. Zhang, and D. Xu, "Enhanced flux-weakening control method for reduced DC-link capacitance IPMSM drives," *IEEE Trans. Power Electron.*, vol. 34, no. 8, pp. 7788–7799, Aug. 2019, doi: 10.1109/TPEL.2018.2878877.

[68] H.-J. Lee and J.-G. Shon, "Improved voltage flux-weakening strategy of permanent magnet synchronous motor in high-speed operation," *Energies*, vol. 14, no. 22, pp. 1–15, Nov. 2021, doi: 10.3390/en14227464.

[69] C. Bianchini, G. Franceschini, and A. Torreggiani, "Improvement on flux weakening control strategy for electric vehicle applications," *Appl. Sci.*, vol. 11, no. 5, pp. 1–16, Mar. 2021, doi: 10.3390/app11052422.

[70] P. Vaclavek and P. Blaha, "Interior permanent magnet synchronous machine field weakening control strategy—The analytical solution," in *Proc. SICE Annu. Conf.*, 2008, pp. 753–757, doi: 10.1109/SICE.2008.4654756.

[71] D. Hu, L. Zhu, and L. Xu, "Maximum torque per volt operation and stability improvement of PMSM in deep flux-weakening region," in *Proc. IEEE Energy Convers. Congr. Expo. (ECCE)*, Sep. 2012, pp. 1233–1237, doi: 10.1109/ECCE.2012.6342675.

[72] H. Liu, Z. Q. Zhu, E. Mohamed, Y. Fu, and X. Qi, "Flux-weakening control of nonsalient pole PMSM having large winding inductance, accounting for resistive voltage drop and inverter nonlinearities," *IEEE Trans. Power Electron.*, vol. 27, no. 2, pp. 942–952, Feb. 2012, doi: 10.1109/TPEL.2011.2159398.

[73] P.-Y. Lin, W.-T. Lee, S.-W. Chen, J.-C. Hwang, and Y.-S. Lai, "Infinite speed drives control with MTPA and MTPV for interior permanent magnet synchronous motor," in *Proc. 40th Annu. Conf. IEEE Ind. Electron. Soc. (IECON)*, Oct. 2014, pp. 668–674, doi: 10.1109/IECON.2014.7048572.

[74] Y. Xu, W. Zhang, and D. Sun, "Comparative research of two flux-weakening method of PMSMs in high speed range," in *Proc. 20th Int. Conf. Electr. Mach. Syst. (ICEMS)*, Aug. 2017, pp. 1–5, doi: 10.1109/ICEMS.2017.8056218.

[75] N. Pothi, "Improvement of flux-weakening control of surface mounted permanent magnet synchronous machine considering inverter nonlinearity," in *Proc. Int. Electr. Eng. Congr. (iEECON)*, Mar. 2017, pp. 1–4, doi: 10.1109/IEECON.2017.8075736.

[76] J. Li, S. Ekanayake, M. F. Rahman, R. Dutta, X. Huang, J. Ma, and Y. Fang, "Deep flux weakening control with six-step overmodulation for a segmented interior permanent magnet synchronous motor," in *Proc. 20th Int. Conf. Electr. Mach. Syst. (ICEMS)*, Aug. 2017, pp. 1–6, doi: 10.1109/ICEMS.2017.8056517.

[77] L. Sepulchre, M. Fadel, M. Pietrzak-David, and G. Porte, "New high speed PMSM flux-weakening strategy," in *Proc. 19th Int. Conf. Electr. Mach. Syst.*, 2016, pp. 1–6.

[78] V. Manzolini, D. D. Rù, and S. Bolognani, "A new control strategy for high efficiency wide speed range synchronous reluctance motor drives," in *Proc. IEEE Int. Electr. Mach. Drives Conf. (IEMDC)*, May 2017, pp. 1–7, doi: 10.1109/IEMDC.2017.8002276.

[79] V. Manzolini, D. D. Rù, and S. Bolognani, "An effective voltage control loop for a deep flux-weakening in IPM synchronous motor drives," in *Proc. IEEE Energy Convers. Congr. Expo. (ECCE)*, Oct. 2017, pp. 3979–3986, doi: 10.1109/ECCE.2017.8096696.

[80] M. Fadel, L. Sepulchre, and M. Pietrzak-David, "Deep flux-weakening strategy with MTPV for high-speed IPMSM for vehicle application," *IFAC-PapersOnLine*, vol. 51, no. 28, pp. 616–621, 2018, doi: 10.1016/j.ifacol.2018.11.772.

[81] L. Sepulchre, M. Fadel, M. Pietrzak-David, and G. Porte, "MTPV flux-weakening strategy for PMSM high speed drive," *IEEE Trans. Ind. Appl.*, vol. 54, no. 6, pp. 6081–6089, Nov. 2018, doi: 10.1109/TIA.2018.2856841.

[82] L. Sepulchre, M. Fadel, and M. Ptetrzak-David, "MTPV for continuous flux-weakening strategy control law for IPMSM," in *Proc. Int. Symp. Power Electron., Electr. Drives, Autom. Motion (SPEEDAM)*, Jun. 2018, pp. 1221–1226, doi: 10.1109/SPEEDAM.2018.8445329.

[83] V. Manzolini, D. D. Rù, and S. Bolognani, "An effective flux weakening control of a SyRM drive including MTPV operation," *IEEE Trans. Ind. Appl.*, vol. 55, no. 3, pp. 2700–2709, May 2019, doi: 10.1109/TIA.2018.2886328.

[84] C. Miguel-Espinar, D. Heredero-Peris, G. Gross, M. Llonch-Masachs, and D. Montesinos-Miracle, "Maximum torque per voltage flux-weakening strategy with speed limiter for PMSM drives," *IEEE Trans. Ind. Electron.*, vol. 68, no. 10, pp. 9254–9264, Oct. 2021, doi: 10.1109/TIE.2020.3020029.

[85] P. Q. Khan and H. P. H. Anh, "Advanced deep flux weakening operation control strategies for IPMSM," *Int. J. Electr. Comput. Eng.*, vol. 11, no. 5, pp. 3798–3808, Oct. 2021, doi: 10.11591/ijece.v11i5.pp3798-3808.

[86] C. Miguel-Espinar, D. Heredero-Peris, O. Subirats-Rillo, X. Escaler, and D. Montesinos-Miracle, "Novel flux-weakening strategy considering the saturation effects for electric vehicles," in *Proc. PCIM Eur. Digit. Days, Int. Exhib. Conf. Power Electron. Intell. Motion, Renew. Energy Energy Manag.*, 2021, pp. 1–8.

[87] W. Peters, T. Huber, and J. Böcker, "Control realization for an interior permanent magnet synchronous motor (IPMSM) in automotive drive trains," in *Proc. PCIM Eur. Conf.*, 2011, pp. 1–6.

[88] T. Huber, W. Peters, and J. Böcker, "Voltage controller for flux weakening operation of interior permanent magnet synchronous motor in automotive traction applications," in *Proc. IEEE Int. Electr. Mach. Drives Conf. (IEMDC)*, May 2015, pp. 1078–1083, doi: 10.1109/IEMDC.2015.7409195.

[89] B.-H. Bae, S.-K. Sul, J.-H. Kwon, and J.-S. Byeon, "Implementation of sensorless vector control for super-high-speed PMSM of turbo-compressor," *IEEE Trans. Ind. Appl.*, vol. 39, no. 3, pp. 811–818, May/Jun. 2003, doi: 10.1109/TIA.2003.810658.

[90] G.-Y. Choi, M.-S. Kwak, T.-S. Kwon, and S.-K. Sul, "Novel flux-weakening control of an IPMSM for quasi six-step operation," in *Proc. IEEE Ind. Appl. Annu. Meeting*, Sep. 2007, pp. 1315–1321, doi: 10.1109/07IAS.2007.204.

[91] T.-S. Kwon, G.-Y. Choi, M.-S. Kwak, and S.-K. Sul, "Novel flux-weakening control of an IPMSM for quasi-six-step operation," *IEEE Trans. Ind. Appl.*, vol. 44, no. 6, pp. 1722–1731, Nov./Dec. 2008, doi: 10.1109/TIA.2008.2006305.

[92] L. Huang, C. Zhao, and P. Huang, "An approach to improve the torque performance of IPMSM by considering cross saturation applied for hybrid electric vehicle," in *Proc. Int. Conf. Electr. Mach. Syst.*, 2010, pp. 1378–1381.

[93] Y. Z. Chen, Y. T. Fang, X. Y. Huang, and J. Zhang, "Torque and flux weakening control with MTPV for interior permanent magnet synchronous motor," in *Proc. IEEE Vehicle Power Propuls. Conf. (VPPC)*, Oct. 2016, pp. 1–5, doi: 10.1109/VPPC.2016.7791804.

[94] S. Ekanayake, J. Fletcher, D. Xiao, M. F. Rahman, and R. Dutta, "Operation along the maximum torque per voltage trajectory in a direct torque and flux controlled interior permanent magnet synchronous motor," in *Proc. 8th IET Int. Conf. Power Electron., Mach. Drives (PEMD)*, 2016, pp. 1–6, doi: 10.1049/cp.2016.0326.

[95] S. Ekanayake, R. Dutta, D. Xiao, and M. F. Rahman, "Direct torque and flux control of a fractional-slot concentrated-winding IPMSM in deep flux-weakening region," in *Proc. 20th Int. Conf. Electr. Mach. Syst. (ICEMS)*, Aug. 2017, pp. 1–6, doi: 10.1109/ICEMS.2017.8056372.
[96] S. Ekanayake, R. Dutta, M. F. Rahman, and D. Xiao, "Direct torque and flux control of interior permanent magnet synchronous machine in deep flux-weakening region," *IET Electr. Power Appl.*, vol. 12, no. 1, pp. 98–105, Sep. 2018, doi: 10.1049/iet-epa.2017.0147.
[97] S. Ekanayake, R. Dutta, F. Rahman, and B. M. Xuan, "Position sensorless control of an interior permanent magnet synchronous machine (IPMSM) in deep flux-weakening region," in *Proc. IEEE 9th Int. Symp. Sensorless Control Electr. Drives (SLED)*, Sep. 2018, pp. 114–119, doi: 10.1109/SLED.2018.8486136.
[98] S. Ekanayake, R. Dutta, M. F. Rahman, and M. X. Bui, "Performances of a fractional-slot concentrated-winding permanent magnet synchronous machine under position sensorless control in deep flux-weakening region," *IEEE Trans. Ind. Appl.*, vol. 55, no. 6, pp. 5938–5946, Nov. 2019, doi: 10.1109/TIA.2019.2931269.
[99] I. Boldea, M. C. Paicu, and G. D. Andreescu, "Active flux concept for motion-sensorless unified AC drives," *IEEE Trans. Power Electron.*, vol. 23, no. 5, pp. 2612–2618, Sep. 2008, doi: 10.1109/TPEL.2008.2002394.
[100] G. Pellegrino, R. I. Bojoi, and P. Guglielmi, "Unified direct-flux vector control for AC motor drives," *IEEE Trans. Ind. Appl.*, vol. 47, no. 5, pp. 2093–2102, Sep. 2011, doi: 10.1109/TIA.2011.2161532.
[101] Y. F. Shi, "Influence of winding resistance on flux-weakening performance of a permanent magnet brushless AC drive," in *Proc. Int. Conf. Power Electron. Mach. Drives*, 2002, pp. 392–397, doi: 10.1049/cp:20020149.
[102] B.-H. Bae, N. Patel, S. Schulz, and S.-K. Sul, "New field weakening technique for high saliency interior permanent magnet motor," in *Proc. 38th IAS Annu. Meeting Conf. Rec. Ind. Appl. Conf.*, 2003, pp. 898–905, doi: 10.1109/IAS.2003.1257641.
[103] M. Kim, J.-S. Yim, S.-K. Sul, and S.-I. Lim, "Implementation of super high-speed permanent magnet synchronous machine drive," in *Proc. IEEE Energy Convers. Congr. Expo.*, Sep. 2009, pp. 1700–1704, doi: 10.1109/ECCE.2009.5316187.

CARLOS MIGUEL-ESPINAR was born in L'Hospitalet de Llobregat, Spain, in 1985. He received the M.Sc. degree in electrical engineering from the Escola Tècnica Superior d'Enginyeria Industrial de Barcelona (ETSEIB), Universitat Politècnica de Catalunya (UPC), in 2011, where he is currently pursuing the Ph.D. degree in advanced control algorithms for PMSMs. Since 2011, he has been a Senior Researcher with the Centre d'Innovació Tecnològica en Convertidors Estàtics i Accionaments (CITCEA), UPC, developing research and development projects for the industry in various areas, such as electronics, power electronics, digital control and communications, and electric machine design.

DANIEL HEREDERO-PERIS was born in Vilanova i la Geltrú, Spain, in 1985. He received the M.Sc. degree in control engineering from the Escola Tècnica Superior d'Enginyeria Industrial de Barcelona (ETSEIB), Universitat Politècnica de Catalunya (UPC), in 2010, where he received the Ph.D. degree, in 2017. Since 2010, he has been with CITCEA, UPC, as a Project Engineer developing tasks focused on the design of algorithms related to the control of grid-connected and standalone single/three-phase inverters, and V2G projects for EV. His main research interests include control of power electronics, micro-grids, and EVs.

ROBERTO VILLAFAFILA-ROBLES (Member, IEEE) was born in Barcelona, Spain, in 1979. He received the M.Sc. degree in electrical engineering, in 2005, and the Ph.D. degree from the Escola Tècnica Superior d'Enginyeria Industrial de Barcelona (ETSEIB), Universitat Politècnica de Catalunya (UPC), in 2009. Since 2003, he has been with CITCEA, UPC, where he is involved in research and development activities and technology transfer with the industry at the local and international levels in the electrical engineering field. Since 2016, he has been a member of the CITCEA Directive Board. He is currently an Associate Professor with the Electrical Engineering Department, UPC. His primary research interests include integrating renewable energy, storage, and electric vehicles into power systems, electrical markets, and energy and territory.

DANIEL MONTESINOS-MIRACLE (Senior Member, IEEE) was born in Barcelona, Spain, in 1975. He received the M.Sc. degree in electrical engineering from the Escola Tècnica Superior d'Enginyeria Industrial de Barcelona (ETSEIB), Universitat Politècnica de Catalunya (UPC), in 2000, where he received the Ph.D. degree, in 2008. In 2001, he joined as a Research and Development Engineer with Salicru Electronics, S.A., Santa Maria de Palautordera, Spain. Since 2001, he has been with CITCEA, UPC, as a Research Collaborator. In 2005, he was a Lecturer with the Electrical Engineering Department, UPC, where he has been an Associate Professor, since 2012. He became the Director of CITCEA, UPC, in 2016. His primary research interests include power electronics, drives, and green energy converters.